

# A conforming sliding mesh technique for an embedded-hybridized discontinuous Galerkin discretization for fluid-rigid body interaction

Tamás L. Horváth<sup>a,1</sup>, Sander Rhebergen<sup>b,2</sup>

<sup>a</sup>*Department of Mathematics and Statistics, Oakland University, U.S.A.*

<sup>b</sup>*Department of Applied Mathematics, University of Waterloo, Canada*

---

## Abstract

In (J. Comput. Phys., 417, 109577, 2020) we introduced a space-time embedded-hybridizable discontinuous Galerkin method for the solution of the incompressible Navier–Stokes equations on time-dependent domains of which the motion of the domain is prescribed. This discretization is exactly mass conserving, locally momentum conserving, and energy-stable. In this manuscript we extend this discretization to fluid-rigid body interaction problems in which the motion of the fluid domain is not known a priori. To account for large rotational motion of the rigid body, we present a novel conforming space-time sliding mesh technique. We demonstrate the performance of the discretization on various numerical examples.

*Keywords:* Navier–Stokes, embedded-hybridized, discontinuous Galerkin, space-time, fluid-rigid body interaction, sliding mesh.

---

## 1. Introduction

In this paper we consider fluid-rigid body interaction problems in which the motion of the rigid body is governed by a system of ordinary differential equations (ODEs) and the fluid problem is governed by the incompressible Navier–Stokes equations. In such problems aerodynamic forces exerted by the fluid at the fluid-rigid body interface results in movement of the rigid body which results in deformation of the fluid domain. Problems of this kind are challenging to solve as the fluid domain, on which the Navier–Stokes equations are defined, is not known a priori. Nevertheless, these problems are of interest in many engineering applications, for example, in simulations of flow around a turbine or modeling the interaction between wind and a bridge.

A popular approach to solve the incompressible Navier–Stokes equations on deforming domains is by using an Arbitrary Eulerian–Lagrangian (ALE) approach in which the deforming domain is mapped to a fixed computational domain. The ALE method has successfully been applied to fluid-rigid body interaction problems (e.g., [1, 2, 3]), a wide variety of fluid-structure interaction problems (e.g., [4, 5, 6, 7]), and free-surface problems (e.g., [8, 9]).

The space-time method, used in the paper, is an alternative to the ALE approach. In a space-time approach a time-dependent partial differential equation (PDE) in  $d$  spatial dimensions is first

---

*Email addresses:* [thorvath@oakland.edu](mailto:thorvath@oakland.edu) (Tamás L. Horváth), [srheberg@uwaterloo.ca](mailto:srheberg@uwaterloo.ca) (Sander Rhebergen)

<sup>1</sup><https://orcid.org/0000-0001-5294-5362>

<sup>2</sup><https://orcid.org/0000-0001-6036-0356>

written as a  $(d + 1)$ -dimensional problem in space-time. One can now naturally discretize a PDE on a deforming domain by noting that a time-dependent domain is ‘fixed’ in space-time.

The space-time problem can be discretized in several ways. For example, in the context of incompressible flows, space-time finite element methods using function spaces that are continuous in space and discontinuous in time have been considered in [10, 11, 12, 13] and discontinuous function spaces in both space and time have been considered in [14, 15, 16, 17]. These methods have successfully been applied to PDEs on deforming domain problems and fluid-structure interaction problems, see, for example, [18, 19, 20, 21].

In this paper we consider function spaces that are discontinuous in space and time. However, unlike space-time DG methods [14, 15, 16, 17], we consider here a space-time embedded-hybridizable discontinuous Galerkin (EHDG) discretization [22]. This discretization is a space-time extension of the hybridizable discontinuous Galerkin (HDG) methods introduced previously in [23, 24, 25] for incompressible flows, and a special case of the space-time HDG discretization (see section 3.1) that was introduced in [26] and analyzed in [27]. Appealing properties of this discretization include that it is exactly mass conserving, locally momentum conserving, and energy-stable. We furthermore remark that the HDG method was first introduced in [28] to reduce the number of globally coupled degrees-of-freedom of usual DG methods. This is achieved by static condensation.

The main focus of this manuscript is the extension of the space-time EHDG method to fluid-rigid body interaction problems in which the rigid body movement results in large deformation of the fluid domain. Large rotational movement of the rigid body may result in a decrease in the quality of the fluid domain mesh, or even mesh entanglement, if the mesh construction is not managed correctly. Therefore, to be able to account for large rotational movement of the rigid body, we consider a sliding mesh approach [29, 30, 31]. For this, we partition the computational fluid mesh into three parts: a rotating mesh, a static mesh, and an annulus mesh. The rigid body is immersed in the rotating mesh. This rotating mesh rotates with the same angular velocity as the body and there is no relative motion between the vertices in this mesh compared to the body. The static mesh, on the other hand, remains fixed and does not deform with the rigid body motion. The annulus mesh is a transition zone between the static mesh and the rotating mesh (see fig. 4). We use edge swapping in the annulus mesh to guarantee a good quality conforming space-time mesh independent of the rotational movement of the rigid body. This is different from [29] in which the annulus mesh results in hanging nodes. We remark that space-time edge swapping was used also in [32]. However, their approach resulted in new mesh connectivity during the simulation. In the current work, we will construct the space-time mesh from building blocks that can be calculated a priori thereby reducing the computational cost that would normally be associated with building new mesh connectivity.

Finally, we remark that the fluid-rigid body interaction problem can be solved either by a staggered or a monolithic approach. In the case of a staggered approach, separate flow (PDE) and structural (ODE) solvers are applied alternately until convergence is reached. Such an approach is used, for example, in [1, 33, 34, 35] and will be used also in this article. In the monolithic approach the coupled ODE and PDE systems are solved simultaneously. We refer to [2, 8, 21, 36, 37] for more details on the monolithic approach.

The rest of this paper is organized as follows. In Sections 2 and 3 we introduce, respectively, the fluid-rigid body interaction problem and its discretization. We discuss the conforming sliding mesh technique in Section 4 and we present numerical examples in Section 5. Finally, conclusions are drawn in Section 6.

## 2. The fluid-rigid body interaction problem

We are interested in the solution of fluid-rigid body interaction in two spatial dimensions and on the time interval  $t \in [0, T]$ . This problem is governed by the incompressible Navier–Stokes equations on a fluid domain coupled to ordinary differential equations that describe translational and rotational displacement of a single rigid body. The fluid domain  $\Omega(t) \subset \mathbb{R}^2$  is time dependent due to the motion of the rigid body. It is therefore convenient to present the Navier–Stokes equations on the space-time domain,

$$\mathcal{E} := \{(t, \mathbf{x}) \mid 0 < t < T, \mathbf{x} \in \Omega(t)\} \subset \mathbb{R}^3. \quad (1)$$

The Navier–Stokes equations for the velocity field  $\mathbf{u} : \mathcal{E} \rightarrow \mathbb{R}^2$  and the kinematic pressure field  $p : \mathcal{E} \rightarrow \mathbb{R}$  are then formulated as:

$$\partial_t \mathbf{u} + \nabla \cdot \boldsymbol{\sigma} = \mathbf{f}, \quad \nabla \cdot \mathbf{u} = 0, \quad \text{in } \mathcal{E}, \quad (2)$$

where  $\mathbf{f} : \mathcal{E} \rightarrow \mathbb{R}^2$  is a forcing term and  $\boldsymbol{\sigma}$  is the momentum flux given by

$$\boldsymbol{\sigma} = \mathbf{u} \otimes \mathbf{u} + p\mathbf{I} - 2\nu\varepsilon(\mathbf{u}), \quad (3)$$

where  $\nu > 0$  is the kinematic viscosity,  $\mathbf{I}$  is the identity tensor, and  $\varepsilon(\mathbf{u}) = (\nabla \mathbf{u} + \nabla \mathbf{u}^T)/2$  is the symmetric part of the velocity gradient.

Denote the space-time outward unit normal to the boundary  $\partial\mathcal{E}$  of the fluid space-time domain  $\mathcal{E}$  by  $(n_t, \mathbf{n}) \in \mathbb{R}^3$ , with temporal component  $n_t \in \mathbb{R}$  and spatial component  $\mathbf{n} \in \mathbb{R}^2$ . This boundary  $\partial\mathcal{E}$  is partitioned into five complementary subsets,  $\partial\mathcal{E}^D$  (the Dirichlet boundary),  $\partial\mathcal{E}^N$  (the Neumann boundary on which  $n_t + \mathbf{u} \cdot \mathbf{n} \geq 0$ ),  $\partial\mathcal{E}^F$  (the free-slip boundary on which we always assume  $n_t = 0$ ),  $\Omega(0)$  (the fluid spatial domain at initial time  $t = 0$ ), and  $\Omega(T)$  (the fluid spatial domain at final time  $t = T$ ). Note that since  $n_t = 0$  on  $\partial\mathcal{E}^F$  we may write  $\partial\mathcal{E}^F = [0, T] \times \partial\Omega^F$ , where  $\partial\Omega^F$  is the part of the boundary of  $\Omega(t)$  on which a free slip boundary is imposed. We then denote by  $\boldsymbol{\tau}$  the unit tangent vector to  $\partial\Omega^F$ . We now prescribe the following boundary conditions:

$$\mathbf{u} = \mathbf{w} \quad \text{on } \partial\mathcal{E}^D, \quad (4a)$$

$$(p\mathbf{I} - 2\nu\varepsilon(\mathbf{u}))\mathbf{n} = \mathbf{g} \quad \text{on } \partial\mathcal{E}^N, \quad (4b)$$

$$\mathbf{u} \cdot \mathbf{n} = 0 \quad \text{on } \partial\mathcal{E}^F, \quad (4c)$$

$$((p\mathbf{I} - 2\nu\varepsilon(\mathbf{u}))\mathbf{n}) \cdot \boldsymbol{\tau} = 0 \quad \text{on } \partial\mathcal{E}^F, \quad (4d)$$

$$\mathbf{u}(0, \mathbf{x}) = \mathbf{u}_0(\mathbf{x}) \quad \text{in } \Omega(0), \quad (4e)$$

where  $\mathbf{g} : \partial\mathcal{E}^N \rightarrow \mathbb{R}^2$  is the prescribed diffusive part of the momentum flux and  $\mathbf{u}_0 : \Omega(0) \rightarrow \mathbb{R}^2$  is the solenoidal initial condition. Furthermore, we partition the Dirichlet boundary into the two complementary sets  $\partial\mathcal{E}^B$  and  $\partial\mathcal{E}^W = \partial\mathcal{E}^D \setminus \partial\mathcal{E}^B$ , where  $\partial\mathcal{E}^B$  is the boundary of the rigid body. Then  $\mathbf{w} : \partial\mathcal{E}^D \rightarrow \mathbb{R}^2$  is prescribed on  $\partial\mathcal{E}^W$  while on  $\partial\mathcal{E}^B$  it is the unknown velocity of the interface  $\mathbf{u}_B$  between the flow and the body.

To determine the interface velocity  $\mathbf{u}_B$  we require the force and moment exerted by the rigid body on the fluid. These are given by, respectively,

$$\mathbf{F}(t) = \int_{\partial\mathcal{E}^B(t)} \rho (p\mathbf{I} - 2\nu\varepsilon(\mathbf{u})) \mathbf{n} \, ds, \quad \mathbf{M}(t) = \int_{\partial\mathcal{E}^B(t)} \Delta \mathbf{x} \times \left[ \rho (p\mathbf{I} - 2\nu\varepsilon(\mathbf{u})) \mathbf{n} \right] \, ds, \quad (5)$$

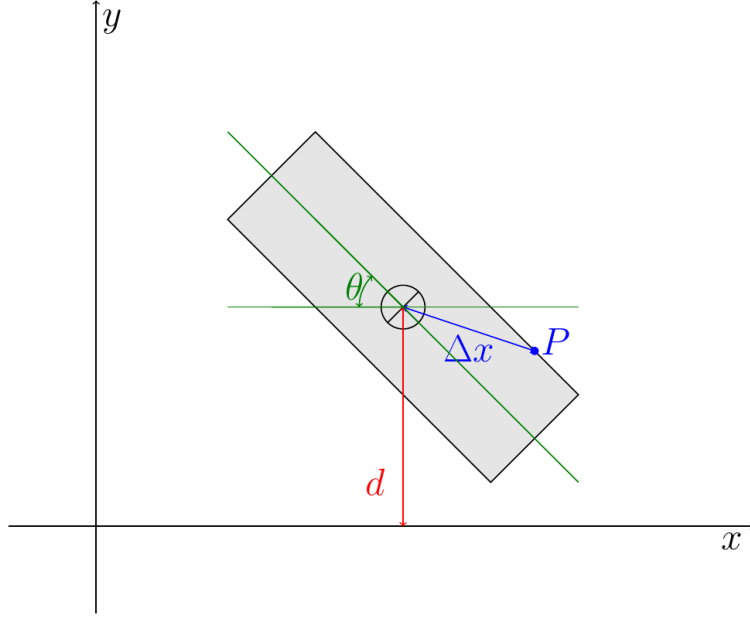


Figure 1: Clarification of notation for the equations describing the motion of a rigid body. The relative position  $\Delta \mathbf{x}$  of a point  $P$  on the surface of the rigid body, the rigid body rotation  $\theta$  are described with respect to the center of gravity of the rectangular rigid body, which is denoted here by  $\otimes$ .

where  $\partial \mathcal{E}^B(t)$  is the fluid-rigid body interface at time  $t$ ,  $\rho$  is a constant density,  $\mathbf{n}$  is the outward normal unit vector of the boundary, and  $\Delta \mathbf{x}$  is the relative position of the surface of the rigid body with respect to its center of gravity. We consider the case where the rigid body translation is displacement only in the  $y$ -direction. We denote this displacement by  $d$ . Denoting the rigid body rotation with respect to the rigid body's center of gravity by  $\theta$  (see fig. 1 for further clarification of the notation), the linear motion of the rigid body is described by

$$m\ddot{d} + c_y\dot{d} + k_y d = F_y, \quad (6a)$$

$$I_\theta \ddot{\theta} + c_\theta \dot{\theta} + k_\theta \theta = M, \quad (6b)$$

where  $m$  is the mass per unit length of the body,  $I_\theta$  is the mass moment of inertia,  $c_y$  and  $c_\theta$  are the damping constants, and  $k_y$  and  $k_\theta$  are the stiffness constants. Furthermore,  $F_y$  is the  $y$ -component of the force vector  $\mathbf{F}$ . The velocity of the interface between the flow and the body,  $\mathbf{u}_B$ , can then be determined from the solution to eq. (6).

### 3. The discretization

#### 3.1. Incompressible Navier–Stokes

To discretize the fluid problem we first discretize the space-time domain  $\mathcal{E}$ . For this we partition the time interval  $[0, T]$  into time levels  $0 = t^0 < t^1 < \dots < t^N = T$  and define the  $n$ th time interval as  $I^n = (t^n, t^{n+1})$  for  $n = 0, \dots, N-1$ . The length of time interval  $I^n$  is denoted by  $\Delta t^n = t^{n+1} - t^n$ . A space-time slab is then defined as

$$\mathcal{E}^n = \{(t, \mathbf{x}) \in \mathcal{E} \mid t \in I^n\}, \quad n = 0, 1, \dots, N-1. \quad (7)$$

It will be useful to partition the boundary  $\partial\mathcal{E}^n$  of a space-time slab  $\mathcal{E}^n$  into the complementary subsets  $\Omega(t^n)$ ,  $\Omega(t^{n+1})$ , and  $\mathcal{Q}^n := \{(t, \mathbf{x}) \in \partial\mathcal{E} \mid t \in I^n\}$ . The discretization of  $\mathcal{E}^n$ , for  $n = 0, \dots, N-1$  is denoted by  $\mathcal{E}_h^n = \cup_{k=1}^M \mathcal{K}_k$ , where  $\mathcal{K}_k$  are space-time simplices. We defer to section 4 for a detailed discussion of creating the mesh. For now we mention that we consider only conforming triangulations. The boundary  $\partial\mathcal{K}$  of a space-time element  $\mathcal{K} \in \mathcal{E}_h^n$  is formed either by  $\mathcal{Q}_{\mathcal{K}}$ ,  $\mathcal{Q}_{\mathcal{K}} \cup K^n$ , or  $\mathcal{Q}_{\mathcal{K}} \cup K^{n+1}$ , where  $\mathcal{Q}_{\mathcal{K}} := \{(t, \mathbf{x}) \in \partial\mathcal{K} \mid t \in I_n\}$ ,  $K^n := \{(t, \mathbf{x}) \in \partial\mathcal{K} \mid t = t^n\}$ , and  $K^{n+1} := \{(t, \mathbf{x}) \in \partial\mathcal{K} \mid t = t^{n+1}\}$ . The outward unit space-time normal vector on the boundary  $\partial\mathcal{K}$  of  $\mathcal{K} \in \mathcal{E}_h^n$  is denoted by  $(n_t, \mathbf{n}) \in \mathbb{R}^3$  where  $n_t$  is the temporal part of the normal and  $\mathbf{n}$  the spatial part. Next, we define an interior facet in the time interval  $I^n$  by  $F := \partial\mathcal{Q}_{\mathcal{K}^+} \cap \partial\mathcal{Q}_{\mathcal{K}^-}$ , where  $\mathcal{K}^-$  and  $\mathcal{K}^+$  are adjacent elements in  $\mathcal{E}_h^n$ , while a boundary facet in the time interval  $I^n$  is a facet of  $\mathcal{Q}_{\mathcal{K}}$  that lies on the boundary. The set and union of all facets in the time interval  $I^n$  are denoted by, respectively,  $\mathcal{F}^n$  and  $\Gamma^n$ .

In each space-time slab  $\mathcal{E}_h^n$  the space-time embedded-hybridized discontinuous Galerkin method results in approximations  $\mathbf{u}_h \in \mathbf{V}_h^n$  to the velocity  $\mathbf{u}$ ,  $\bar{\mathbf{u}}_h \in \bar{\mathbf{V}}_h^n(\mathbf{w})$  to the trace of the velocity on element boundaries,  $p_h \in Q_h^n$  to the pressure  $p$ , and  $\bar{p}_h \in \bar{Q}_h^n$  to the trace of the pressure on element boundaries. Here the ‘velocity’ finite element spaces are defined as

$$\mathbf{V}_h^n := \{\mathbf{v}_h \in [L^2(\mathcal{E}_h^n)]^2 \mid \mathbf{v}_h \in [P_k(\mathcal{K})]^2 \quad \forall \mathcal{K} \in \mathcal{E}_h^n\}, \quad (8a)$$

$$\begin{aligned} \bar{\mathbf{V}}_h^n(\mathbf{w}) := \{\bar{\mathbf{v}}_h \in [L^2(\mathcal{F}^n)]^2 \mid \bar{\mathbf{v}}_h \in [P_k(F)]^2 \quad \forall F \in \mathcal{F}^n, \bar{\mathbf{v}}_h = \mathbf{w} \text{ on } \partial\mathcal{E}^D \cap \partial\mathcal{E}^n, \\ \bar{\mathbf{v}}_h \cdot \mathbf{n} = 0 \text{ on } \partial\mathcal{E}^F \cap \partial\mathcal{E}^n\} \cap C(\Gamma^n), \end{aligned} \quad (8b)$$

where  $P_l(D)$  denotes the space of polynomials of degree  $l \geq 0$  on a domain  $D$ . The ‘pressure’ finite element spaces are defined as

$$Q_h^n := \{q_h \in L^2(\mathcal{E}_h^n) \mid q_h \in P_{k-1}(\mathcal{K}) \quad \forall \mathcal{K} \in \mathcal{E}_h^n\}, \quad (9a)$$

$$\bar{Q}_h^n := \{\bar{q}_h \in L^2(\mathcal{F}) \mid \bar{q}_h \in P_k(F) \quad \forall F \in \mathcal{F}^n\}. \quad (9b)$$

Note that the space-time EHDG method approximates the trace of the velocity using a continuous facet space but that the trace of the pressure is approximated in a discontinuous facet space. We remark, however, that with minimal changes to the space-time EHDG discretization it is possible to obtain also a space-time HDG (in which both facet spaces are discontinuous) and a space-time EDG (in which both facet spaces are continuous) discretization of the fluid-rigid body interaction problem. See [22] for a detailed comparison of the three methods.

The space-time EHDG discretization of the momentum and continuity equations eq. (2) in each space-time slab  $\mathcal{E}_h^n$ ,  $n = 0, \dots, N-1$ , is now given by [26, 22]: find  $(\mathbf{u}_h, \bar{\mathbf{u}}_h) \in \mathbf{V}_h^n \times \bar{\mathbf{V}}_h^n(\mathbf{w})$  and  $(p_h, \bar{p}_h) \in Q_h^n \times \bar{Q}_h^n$  such that

$$\begin{aligned} & - \sum_{\mathcal{K} \in \mathcal{E}_h^n} \int_{\mathcal{K}} (\mathbf{u}_h \partial_t \mathbf{v}_h + \boldsymbol{\sigma}_h : \nabla \mathbf{v}_h) \, d\mathbf{x} \, dt + \sum_{\mathcal{K} \in \mathcal{E}_h^n} \int_{\mathcal{Q}_{\mathcal{K}}} \hat{\boldsymbol{\sigma}}_h \cdot (\mathbf{v}_h - \bar{\mathbf{v}}_h) \, ds + \int_{\Omega(t_{n+1})} \mathbf{u}_h \cdot \mathbf{v}_h \, d\mathbf{x} \\ & - \sum_{\mathcal{K} \in \mathcal{E}_h^n} \int_{\mathcal{Q}_{\mathcal{K}}} 2\nu \boldsymbol{\varepsilon}(\mathbf{v}_h) : (\mathbf{u}_h - \bar{\mathbf{u}}_h) \otimes \mathbf{n} \, ds + \int_{\partial\mathcal{E}^N \cap I_n} (n_t + \bar{\mathbf{u}}_h \cdot \mathbf{n}) \bar{\mathbf{u}}_h \cdot \bar{\mathbf{v}}_h \, ds \\ & = \sum_{\mathcal{K} \in \mathcal{E}_h^n} \int_{\mathcal{K}} \mathbf{f} \cdot \mathbf{v}_h \, d\mathbf{x} \, dt - \int_{\partial\mathcal{E}^N \cap I_n} \mathbf{g} \cdot \bar{\mathbf{v}}_h \, ds + \int_{\Omega(t_n)} \mathbf{u}_h^- \cdot \mathbf{v}_h \, d\mathbf{x}, \end{aligned} \quad (10a)$$

for all  $(\mathbf{v}_h, \bar{\mathbf{v}}_h) \in \mathbf{V}_h^n \times \bar{\mathbf{V}}_h^n(\mathbf{0})$  and

$$- \sum_{\mathcal{K} \in \mathcal{E}_h^n} \int_{\mathcal{K}} q_h \nabla \cdot \mathbf{u}_h \, d\mathbf{x} \, dt + \sum_{\mathcal{K} \in \mathcal{E}_h^n} \int_{\mathcal{Q}_{\mathcal{K}}} (\mathbf{u}_h - \bar{\mathbf{u}}_h) \cdot \mathbf{n} \bar{q}_h \, ds = 0, \quad (10b)$$

for all  $(q_h, \bar{q}_h) \in Q_h^n \times \bar{Q}_h^n$ . When  $n = 0$ ,  $\mathbf{u}_h^-$  is the projection of the initial condition  $\mathbf{u}_0$  into  $\mathbf{V}_h^0 \cap H(\text{div})$  such that  $\nabla \cdot \mathbf{u}_h^- = 0$  element-wise. When  $n > 0$ ,  $\mathbf{u}_h^- = \lim_{\varepsilon \rightarrow 0} \mathbf{u}_h(t^n - \varepsilon)$ . Furthermore,  $\hat{\boldsymbol{\sigma}}_h$  is an approximation to the normal component of the momentum flux on element boundaries, which is given by

$$\hat{\boldsymbol{\sigma}}_h := (n_t + \mathbf{u}_h \cdot \mathbf{n})(\mathbf{u}_h + \lambda(\bar{\mathbf{u}}_h - \mathbf{u}_h)) + (\bar{p}_h \mathbf{I} - 2\nu \boldsymbol{\varepsilon}(\mathbf{u}_h)) \mathbf{n} + \frac{2\nu\alpha}{h_{\mathcal{K}}}(\mathbf{u}_h - \bar{\mathbf{u}}_h), \quad (11)$$

where  $\lambda = 1$  when  $(n_t + \mathbf{u}_h \cdot \mathbf{n}) < 0$  and  $\lambda = 0$  when  $(n_t + \mathbf{u}_h \cdot \mathbf{n}) \geq 0$ ,  $\alpha > 0$  is a penalty parameter that needs to be sufficiently large to ensure stability, and  $h_{\mathcal{K}}$  is the characteristic length of the element  $\mathcal{K}$ . We remark that the advective part of this numerical flux is a space-time upwind flux while the diffusive part is an interior penalty flux.

In [26, 22] we proved that the space-time EHDG discretization eq. (10) results in an approximate velocity field  $\mathbf{u}_h$  that is exact divergence-free and  $H(\text{div})$ -conforming on space-time elements, i.e.,  $\nabla \cdot \mathbf{u}_h = 0$  for  $(t, \mathbf{x}) \in \mathcal{K}$  for all  $\mathcal{K} \in \mathcal{E}_h^n$ ,  $\mathbf{u}_h \cdot \mathbf{n}$  is single-valued on interior faces and  $\mathbf{u}_h \cdot \mathbf{n} = \bar{\mathbf{u}}_h \cdot \mathbf{n}$  on boundary faces. A consequence of these results is that the discretization is exactly mass conserving and that the discretization is both locally conservative and energy stable, even on deforming domains.

The space-time EHDG discretization eq. (10) in space-time slab  $\mathcal{E}_h^n$ ,  $n = 0, \dots, N-1$ , results in a nonlinear system of algebraic equations. To solve this nonlinear problem we use Picard iterations: given  $(\mathbf{u}_h^k, \bar{\mathbf{u}}_h^k) \in \mathbf{V}_h^n \times \bar{\mathbf{V}}_h^n(\mathbf{w})$  we seek  $(\mathbf{u}_h^{k+1}, \bar{\mathbf{u}}_h^{k+1}) \in \mathbf{V}_h^n \times \bar{\mathbf{V}}_h^n(\mathbf{w})$  and  $(p_h^{k+1}, \bar{p}_h^{k+1}) \in Q_h^n \times \bar{Q}_h^n$  such that

$$\begin{aligned} & - \sum_{\mathcal{K} \in \mathcal{E}_h^n} \int_{\mathcal{K}} (\mathbf{u}_h^{k+1} \partial_t \mathbf{v}_h + \boldsymbol{\sigma}_h^k : \nabla \mathbf{v}_h) \, d\mathbf{x} \, dt + \sum_{\mathcal{K} \in \mathcal{E}_h^n} \int_{\mathcal{Q}_{\mathcal{K}}} \hat{\boldsymbol{\sigma}}_h^k \cdot (\mathbf{v}_h - \bar{\mathbf{v}}_h) \, ds + \int_{\Omega(t_{n+1})} \mathbf{u}_h^{k+1} \cdot \mathbf{v}_h \, d\mathbf{x} \\ & - \sum_{\mathcal{K} \in \mathcal{E}_h^n} \int_{\mathcal{Q}_{\mathcal{K}}} 2\nu \boldsymbol{\varepsilon}(\mathbf{v}_h) : (\mathbf{u}_h^{k+1} - \bar{\mathbf{u}}_h^{k+1}) \otimes \mathbf{n} \, ds + \int_{\partial \mathcal{E}^N \cap I_n} (n_t + \bar{\mathbf{u}}_h^k \cdot \mathbf{n}) \bar{\mathbf{u}}_h^{k+1} \cdot \bar{\mathbf{v}}_h \, ds \\ & = \sum_{\mathcal{K} \in \mathcal{E}_h^n} \int_{\mathcal{K}} \mathbf{f} \cdot \mathbf{v}_h \, d\mathbf{x} \, dt - \int_{\partial \mathcal{E}^N \cap I^n} \mathbf{g} \cdot \bar{\mathbf{v}}_h \, ds + \int_{\Omega(t_n)} \mathbf{u}_h^- \cdot \mathbf{v}_h \, d\mathbf{x}, \end{aligned} \quad (12a)$$

for all  $(\mathbf{v}_h, \bar{\mathbf{v}}_h) \in \mathbf{V}_h^n \times \bar{\mathbf{V}}_h^n(\mathbf{0})$  and

$$- \sum_{\mathcal{K} \in \mathcal{E}_h^n} \int_{\mathcal{K}} q_h \nabla \cdot \mathbf{u}_h^{k+1} \, d\mathbf{x} \, dt + \sum_{\mathcal{K} \in \mathcal{E}_h^n} \int_{\mathcal{Q}_{\mathcal{K}}} (\mathbf{u}_h^{k+1} - \bar{\mathbf{u}}_h^{k+1}) \cdot \mathbf{n} \bar{q}_h \, ds = 0, \quad (12b)$$

for all  $(q_h, \bar{q}_h) \in Q_h^n \times \bar{Q}_h^n$  for  $k = 0, 1, 2, \dots$ . Here  $\boldsymbol{\sigma}_h^k$  and  $\hat{\boldsymbol{\sigma}}_h^k$  are the following modifications of, respectively, eqs. (3) and (11):

$$\begin{aligned} \boldsymbol{\sigma}_h^k &= \mathbf{u}_h^k \otimes \mathbf{u}_h^{k+1} + p_h^{k+1} \mathbf{I} - 2\nu \boldsymbol{\varepsilon}(\mathbf{u}_h^{k+1}), \\ \hat{\boldsymbol{\sigma}}_h^k &= (n_t + \mathbf{u}_h^k \cdot \mathbf{n})(\mathbf{u}_h^{k+1} + \lambda(\bar{\mathbf{u}}_h^{k+1} - \mathbf{u}_h^{k+1})) + (\bar{p}_h^{k+1} \mathbf{I} - 2\nu \boldsymbol{\varepsilon}(\mathbf{u}_h^{k+1})) \mathbf{n} + \frac{2\nu\alpha}{h_{\mathcal{K}}}(\mathbf{u}_h^{k+1} - \bar{\mathbf{u}}_h^{k+1}). \end{aligned}$$

To initialize the Picard iteration we set  $\mathbf{u}_h^0 = 0$  on all elements in  $\mathcal{E}_h^n$ ,  $\bar{\mathbf{u}}_h^0 = \mathbf{w}$  on Dirichlet boundary facets, and  $\bar{\mathbf{u}}_h^0 = 0$  on all remaining facets in  $\mathcal{F}^n$ . As stopping criterion we use

$$\max \left\{ \frac{\|\mathbf{u}_h^{k+1} - \mathbf{u}_h^k\|_\infty}{\|\mathbf{u}_h^{k+1} - \mathbf{u}_h^0\|_\infty}, \frac{\|p_h^{k+1} - p_h^k\|_\infty}{\|p_h^{k+1} - p_h^0\|_\infty} \right\} < \delta_{\text{NS}}, \quad (13)$$

where  $\|\cdot\|_\infty$  is the discrete maximum-norm and  $\delta_{\text{NS}}$  is the desired tolerance. Once the convergence criterion is met we set  $(\mathbf{u}_h, \mathbf{p}_h) = (\mathbf{u}_h^{k+1}, \mathbf{p}_h^{k+1})$ .

### 3.2. Rigid body time integration

In this section we discretize the equations that describe the motion of the rigid body eq. (6). Since the discretization for eq. (6a) and eq. (6b) are similar, we present here only the details for eq. (6a).

We write the second-order ordinary differential equation eq. (6a) as the following first-order system:

$$\dot{d} = b, \quad \dot{b} = (-k_y d - c_y b + F_y)/m. \quad (14)$$

We then discretize eq. (14) by a predictor-corrector method. In particular, starting from the initial condition  $(d_0, b_0)$ , we generate the values  $(d_{n+1}, b_{n+1})$  for  $n = 0, 1, \dots, N-1$  using the following algorithm. In the predictor step we first calculate an initial guess  $(d_{n+1}^0, b_{n+1}^0)$  using Euler's method:

$$d_{n+1}^0 = \Delta t^n b_n + d_n, \quad (15a)$$

$$b_{n+1}^0 = \Delta t^n (-k_y d_n - c_y b_n + F_y(t_n)) / m + b_n. \quad (15b)$$

We then update the initial guess in the corrector step to  $(d_{n+1}^l, b_{n+1}^l)$  for  $l = 1, 2, \dots$  until a stopping criterion is met. These updates are given by a BDF2 discretization:

$$d_{n+1}^l = \frac{2}{3} \Delta t^n b_{n+1}^{l-1} + \frac{4}{3} d_n - \frac{1}{3} d_{n-1}, \quad (16a)$$

$$b_{n+1}^l = \frac{2}{3} \Delta t^n (-k_y d_{n+1}^{l-1} - c_y b_{n+1}^{l-1} + F_y(t_{n+1})) / m + \frac{4}{3} b_n - \frac{1}{3} b_{n-1}. \quad (16b)$$

We use the following stopping criterion:

$$\sqrt{(d_{n+1}^l - d_{n+1}^{l-1})^2 + (b_{n+1}^l - b_{n+1}^{l-1})^2} < \delta_{\text{rb}}, \quad (17)$$

where  $\delta_{\text{rb}}$  is the desired tolerance. When the stopping criterion is met, we define  $(d_{n+1}, b_{n+1})$  as the last corrector step.

The interface velocity between the fluid and the body,  $\mathbf{u}_B$ , is updated at every iteration using  $(d_{n+1}^l, b_{n+1}^l)$  and  $(\theta_{n+1}^l, \kappa_{n+1}^l)$ , where  $(\theta_{n+1}^l, \kappa_{n+1}^l)$  is an approximation to  $(\theta(t^{n+1}), \dot{\theta}(t^{n+1}))$ .

### 3.3. Staggered coupling for fluid-rigid body interaction

Given the discretization of the fluid problem and the equations describing the motion of the rigid body in, respectively, sections 3.1 and 3.2, we now briefly discuss the coupling of these discretizations when advancing from  $t^n$  to  $t^{n+1}$ .

Given the velocity and pressure solution at time  $t = t^n$ , we first estimate the rigid body movement by eq. (15) after which we update the flow domain and the mesh  $\mathcal{E}_h^n$ . Given the new

mesh, we solve the flow equations by Picard iteration eq. (12) until eq. (13) is satisfied. The updated velocity and pressure solutions are then used to calculate the forces eq. (5) after which we apply the corrector step eq. (16). If we satisfy eq. (17), we move to the next time slab; otherwise, we again update the flow domain and solve the fluid problem. See algorithm 1.

---

**Algorithm 1** Staggered coupling for fluid-rigid body solver in space-time slab  $\mathcal{E}_h^n$ .

---

- 1: Predictor step eq. (15) to obtain an initial guess for the rigid body position
  - 2: **while** Rigid body stopping criterion eq. (17) not satisfied **do**
  - 3:     Update the flow domain and mesh  $\mathcal{E}_h^n$
  - 4:     **while** Picard stopping criterion eq. (13) not satisfied **do**
  - 5:         Solve eq. (12) to obtain the flow solution  $(\mathbf{u}_h^{k+1}, \bar{\mathbf{u}}_h^{k+1}, p_h^{k+1}, \bar{p}_h^{k+1})$
  - 6:     **end while**
  - 7:     Set  $(\mathbf{u}_h, \bar{\mathbf{u}}_h, p_h, \bar{p}_h) = (\mathbf{u}_h^{k+1}, \bar{\mathbf{u}}_h^{k+1}, p_h^{k+1}, \bar{p}_h^{k+1})$
  - 8:     Corrector step eq. (16) to update the rigid body position
  - 9: **end while**
- 

#### 4. A conforming sliding mesh technique

Due to the fluid-rigid body interaction, an update of the flow domain/mesh  $\mathcal{E}_h^n$  is required in each space-time slab (see line 3 of algorithm 1). However, for some problems the rotational motion and displacement of the rigid body can be large which may result in mesh entanglement if the flow domain is not re-meshed. To account for large deformation of the domain we therefore consider here a conforming sliding mesh technique.

In this section we will first discuss the extension of a triangular spatial mesh to a tetrahedral space-time mesh after which we explain the necessary edge swapping to obtain a conforming sliding mesh. We will assume that the number of spatial elements  $K^n$  is constant for all  $n = 0, \dots, N$  and we will denote the (global) identifiers of the three vertices of an element  $K^n$  by  $p_i^n$  with  $i \in \{1, \dots, N_v\}$  with  $N_v$  the total number of vertices in the spatial mesh.

##### 4.1. Tetrahedral space-time mesh generation

Let  $\Omega_h(t^n) := \cup_{j=1}^J K_j^n$  be the discretization of the spatial domain  $\Omega(t)$  at time level  $t = t^n$ , with  $J$  the total number of elements in the spatial mesh, and let  $\mathbf{x}_i^{j,n}$ ,  $i = 1, 2, 3$ , be the spatial coordinates of the vertices of a spatial element  $K_j^n$ . Furthermore, let  $\Phi^n : \Omega_h(t^n) \rightarrow \Omega_h(t) : \mathbf{x} \mapsto \Phi^n(\mathbf{x})$  be the mapping that represents the evolution of the spatial domain due to the fluid-rigid body interaction from  $t^n$  to  $t^{n+1}$ . Following [38], the spatial elements  $K_j^{n+1}$  at time level  $t = t^{n+1}$  are obtained from  $K_j^n$  by moving the vertices  $\mathbf{x}_i^{j,n}$  to their new position at time level  $t = t^{n+1}$  using the mapping  $\Phi^n$ . We remark that if the vertex  $\mathbf{x}_i^{j,n}$  has global identifier  $p_j^n$ , then the vertex  $\mathbf{x}_i^{j,n+1} = \Phi^n(\mathbf{x}_i^n)$  has global identifier  $p_j^{n+1} = p_j^n + N_v$ . A space-time element can then be obtained by connecting  $K_j^n$  and  $K_j^{n+1}$  via linear interpolation in time. For ease of discussion we call this space-time element a space-time ‘prism’ but remark that, depending on the mapping  $\Phi^n$ , this prism may not have flat quadrilateral sides. In our discretization, however, we never create a space-time mesh consisting of prisms. Instead, the space-time prisms are used as an intermediate step to create a space-time mesh consisting only of tetrahedra. This is because our space-time EHDG discretization eq. (10) is exactly mass conserving, locally momentum conservative, and



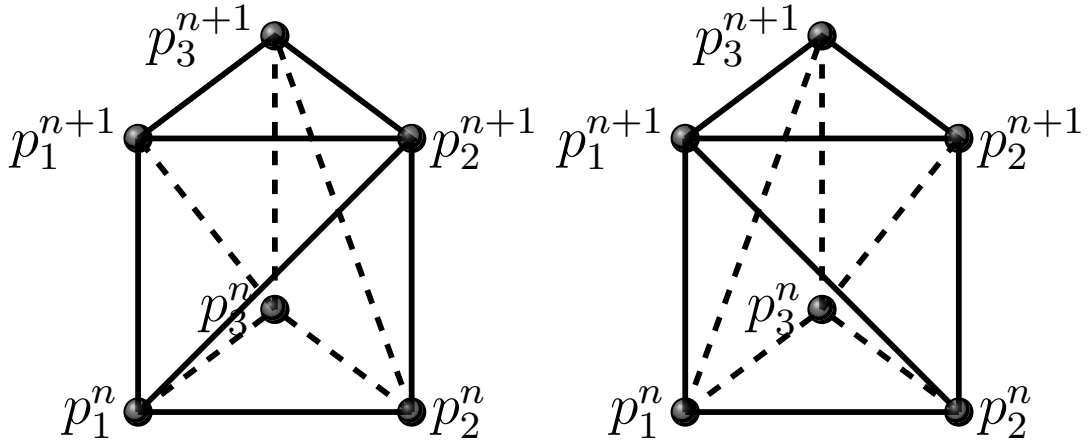


Figure 2: Invalid cuts of a prism.

energy-stable on simplicial meshes (see [26, 22]). A further consequence of cutting the prisms into tetrahedra is that all boundary sides of the space-time tetrahedra are flat surfaces.

There are six different ways to cut a prism into three tetrahedra and these can be identified by the way the quadrilateral sides of a prism are cut (see [32]). To identify these different cuts, let us call a set of diagonal cuts of the quadrilateral sides *valid* if they generate three tetrahedra. The three quadrilateral sides of a prism can be cut along either of the two diagonals resulting in  $2^3$  possible ways to cut a prism. Only six of these cuts, however, are valid and these are the cuts where two of the quadrilateral diagonals share a vertex. The two invalid cuts are shown in fig. 2.

A valid cut is guaranteed by using the quadrilateral diagonal starting at the vertex with the smallest identifier on every quadrilateral side; this vertex is included in two quadrilateral cuts (see fig. 3). This approach generates a conforming tetrahedral mesh since the quadrilateral side shared by two neighboring prisms is divided into two triangles for both prisms in the same way.

#### 4.2. Edge swapping

In this paper, we consider sliding meshes to account for large deformation of the flow domain. Following for example [29], we consider a mesh where an inner mesh rotates with respect to an outer static mesh (see fig. 4). Different from [29], however, is that we consider edge swapping in the annulus separating the static and rotating mesh to avoid hanging nodes. This preserves exact mass conservation of our EHDG discretization and furthermore has the advantage that we do not require internal curved edges. In this section we explain the edge swapping to obtain a conforming space-time sliding mesh in the time interval  $[t^n, t^{n+1}]$ .

The spatial mesh at time level  $t = t^n$  is fixed since it is the upper boundary of the space-time mesh  $\mathcal{E}_h^{n-1}$  from the previous time interval  $[t^{n-1}, t^n]$ . Consider therefore the spatial mesh at time  $t = t^{n+1}$ . Initially, we consider this to be a mixed mesh consisting of quadrilaterals in the annulus that separates the inner and outer mesh, and triangles elsewhere. The annulus itself is separated into two layers of elements resulting in an inner annulus, which we refer to as the buffer layer, and an outer annulus, which we refer to as the sliding layer (see fig. 4). When the inner mesh rotates, all vertices in the annulus move except the vertices shared also by the outer static mesh.

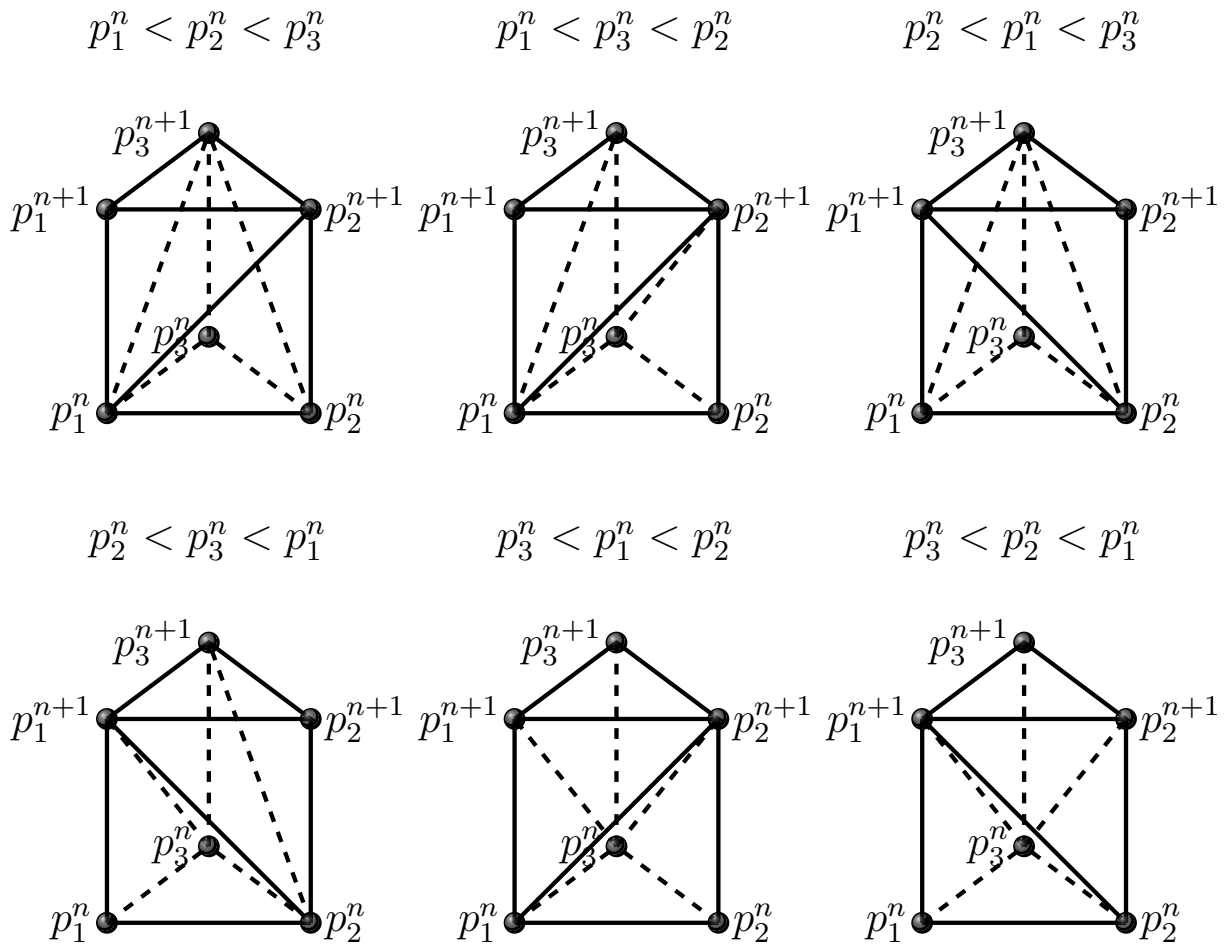


Figure 3: Valid cuts of a prism.

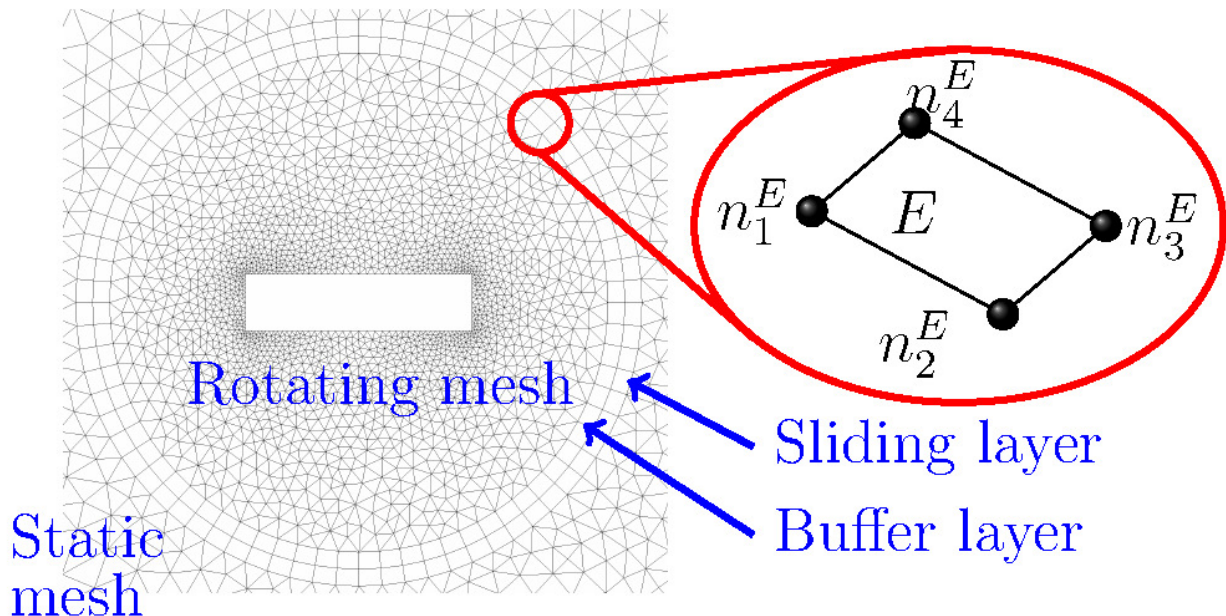


Figure 4: The initial mixed spatial mesh and the numbering of the quadrilateral nodes.

In the initial mesh we will require an even number of quadrilaterals in the buffer and that the number of quadrilaterals in the buffer and sliding layers are equal.

Consider now a quadrilateral  $E$  in the spatial mesh at time  $t = t^{n+1}$  with vertices  $n_i^E$ ,  $i = 1, \dots, 4$ . We introduce the following numbering convention:  $n_1^E$  and  $n_2^E$  are the vertices closest to the center of rotation and ordered clockwise on the annulus while the remaining two vertices  $n_3^E$  and  $n_4^E$  are ordered anticlockwise with respect to the center of the quadrilateral (see fig. 4). Since we are interested in generating a tetrahedral space-time mesh on the whole domain (see section 4.1), we next cut the quadrilaterals along their  $n_2^E - n_4^E$  diagonals to obtain a triangular mesh on the whole spatial domain. These diagonal cuts now form a secondary quadrilateral mesh in the sliding layer. For example, the quadrilaterals  $\{p_6^{n+1}, p_7^{n+1}, p_{13}^{n+1}, p_{14}^{n+1}\}$  and  $\{p_7^{n+1}, p_8^{n+1}, p_{12}^{n+1}, p_{13}^{n+1}\}$  in fig. 5(i) are elements in a secondary quadrilateral mesh. Note that cutting quadrilaterals in the secondary mesh along the  $n_1^E - n_3^E$  diagonal results in the same simplicial mesh as cutting quadrilaterals in the primary mesh along the  $n_2^E - n_4^E$  diagonal.

Rotation of the inner mesh may result in triangles in the sliding layer of which their inscribed circles have a small radius thereby resulting in a low quality spatial mesh at time  $t = t^{n+1}$ . This can be avoided, however, by edge swapping. The edge swapping can occur on the initial quadrilateral mesh or on the secondary quadrilateral mesh. Consider, for example, fig. 5(ii). Here we would swap the diagonals of the initial quadrilateral mesh, i.e., we would replace  $p_6^{n+1} - p_{14}^{n+1}$  by  $p_5^{n+1} - p_{13}^{n+1}$ , and similarly for the other quadrilaterals. In the case of fig. 5(iii), however, we would swap the diagonal of the secondary quadrilateral mesh, i.e., we would replace  $p_6^{n+1} - p_{13}^{n+1}$  by  $p_7^{n+1} - p_{14}^{n+1}$ , and similarly for the remaining quadrilaterals of the secondary mesh. Note that the same diagonal cut is used in all elements in the sliding layer. To determine whether edge swapping is necessary in the sliding layer, we therefore need to compute the diagonals only of one quadrilateral element in the primary mesh and of one quadrilateral in the secondary mesh. We always choose the mesh built

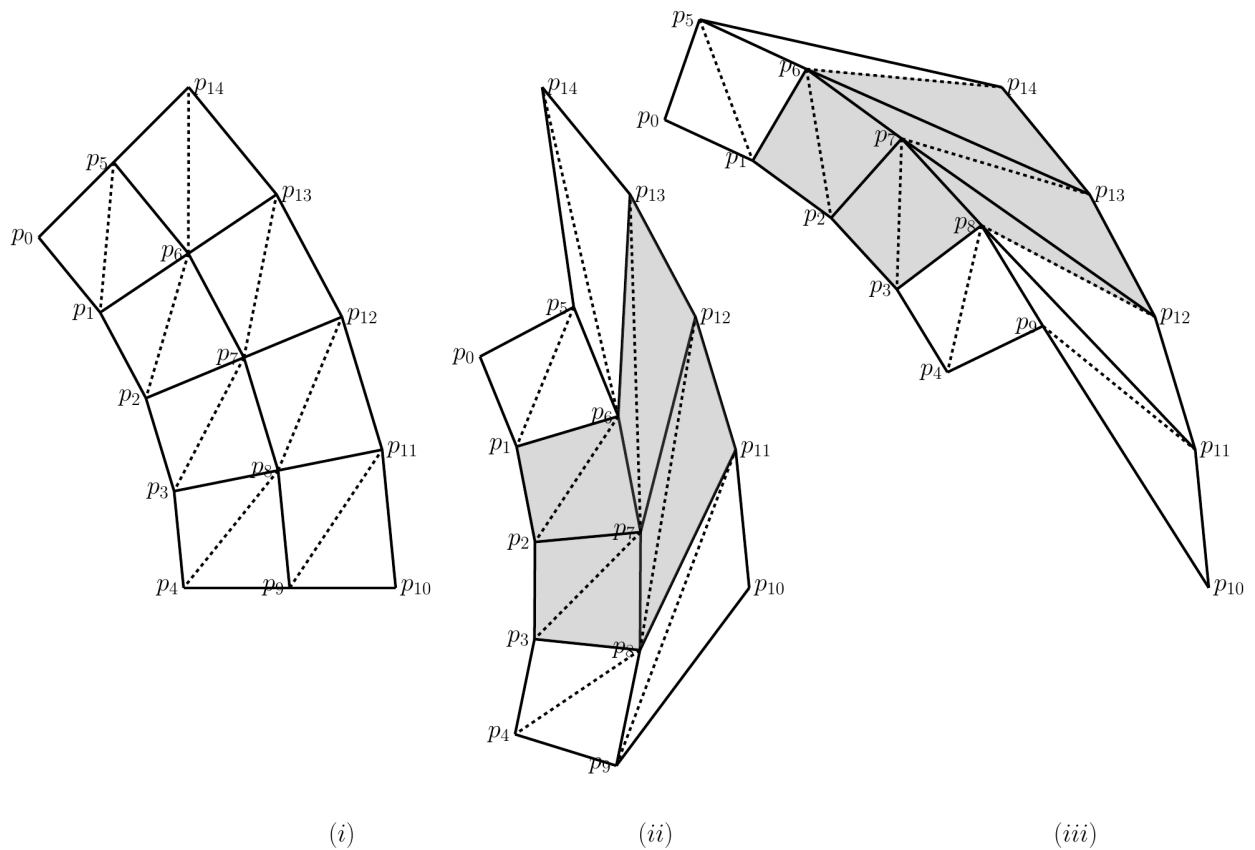


Figure 5: Here we show part of the triangular mesh in the sliding layer. In (i) we show part of this mesh before rotation. In (ii) and (iii) we show part of this mesh once the inner mesh has started to rotate. In (ii) edge swapping is necessary in the quadrilaterals of the initial quadrilateral mesh. In (iii) edge swapping is necessary in the quadrilaterals of the secondary quadrilateral mesh.

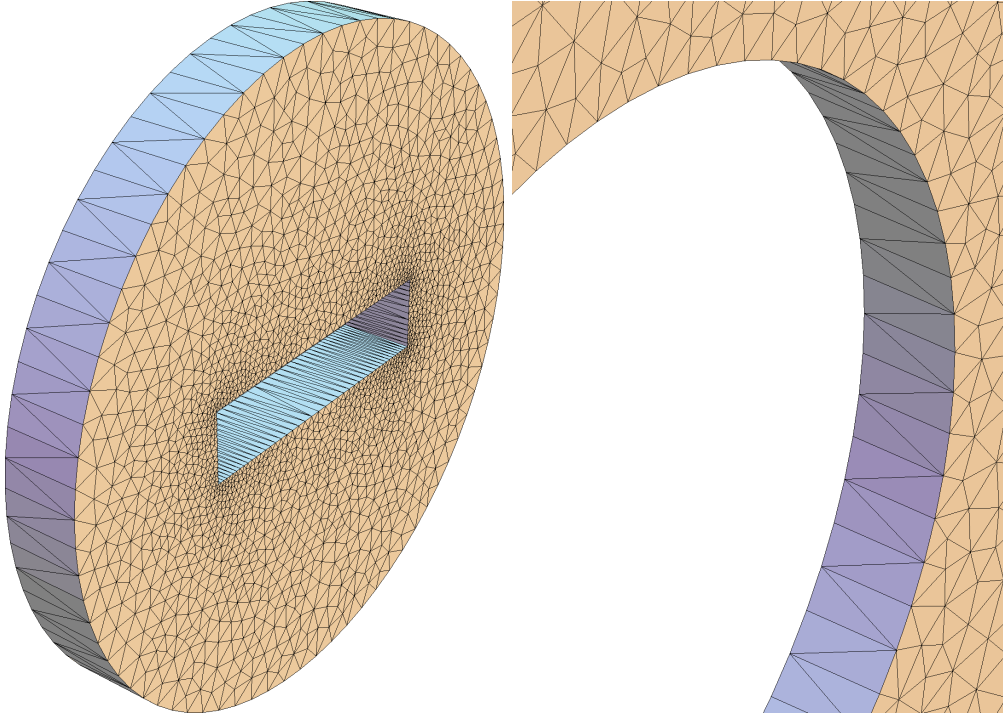


Figure 6: On the outer boundary of the rotating space-time inner mesh (left) and on the inner boundary the outer space-time static mesh (right) we observe a ‘chainsaw’ pattern.

from quadrilaterals with the shortest diagonal in the sliding layer; if the shortest diagonal appears in the current mesh, no edge swapping is necessary, otherwise it is. There is no edge swapping in the buffer layer.

Given the spatial mesh at times  $t = t^n$  and  $t = t^{n+1}$ , we next construct the space-time tetrahedral mesh. At this point we remark that  $p_j^n$  is always connected to  $p_j^{n+1}$  by linear interpolation in time (see section 4.1) and that the connectivity in the inner rotating mesh and in the outer static mesh do not change throughout the simulation. If no edge swapping takes place at  $t = t^{n+1}$  we can directly use the algorithm from section 4.1. Otherwise, we note that there are only four different connectivity sets for the space-time mesh of the annulus when edge swapping does take place and these can be calculated before the start of a simulation. During the simulation, in each space-time slab, we then only need to choose one of the four connectivity sets. We discuss this next.

To construct the space-time mesh, consider again the annulus in fig. 4. The boundary of this annulus consists of the inner boundary circle and the outer boundary circle. For ease of discussion, we now introduce the following numbering of the vertices on the inner boundary circle: no three adjacent vertices are in an increasing or decreasing order, i.e., for any three adjacent vertices, the identifier of the middle vertex is either smaller or larger than its two neighboring vertices. We use the same numbering rule for the vertices on the outer boundary circle. This numbering of the vertices combined with the tetrahedral space-time mesh generation algorithm of section 4.1 for the rotating space-time inner mesh and the outer space-time static mesh, results in a ‘chainsaw’ pattern on the outer boundary of the inner mesh and on the inner boundary of the outer mesh, see fig. 6.

Cut 1	Cut 2	Cut 5	Cut 6	Cut 1	Cut 2	Cut 5	Cut 6
Cut 3	Cut 4	Cut 3	Cut 4	Cut 7	Cut 8	Cut 7	Cut 8
Configuration 1		Configuration 2		Configuration 3		Configuration 4	

Table 1: The four different hexahedral cut configurations to create a conforming tetrahedral mesh over the sliding and buffer layers. See fig. 7 for the different cuts.

The space-time mesh generated in the annulus now has to match these chainsaw patterns so that the space-time facets of the outer boundary of the rotating space-time inner mesh match with the space-time facets of the inner boundary of the space-time annulus. Likewise, the space-time facets of the inner boundary of the outer space-time static mesh have to match with the space-time facets of the outer boundary of the space-time annulus. The remaining space-time facets of the tetrahedral space-time mesh in the interior of the annulus now provide enough freedom to construct a conforming space-time mesh, as described next.

Consider the space-time extension from  $t^n$  to  $t^{n+1}$  of a  $2 \times 2$  block of quadrilaterals in the annulus of which two are adjacent elements in the sliding layer and the other two are their neighbors in the buffer layer. Note that this space-time extension may not result in a space-time hexahedra as not all faces may be flat space-time quadrilaterals. However, similar to the algorithm described in section 4.1, we never create a space-time hexahedra; it is used only as an intermediate step to create space-time tetrahedra. To simplify the discussion we therefore refer to this space-time extension as a space-time hexahedra with space-time quadrilateral sides. To continue, let us denote the space-time quadrilateral side of a space-time hexahedron in the buffer layer that is shared by the inner mesh by  $S_{in}$  (shaded gray in the bottom row of fig. 7) and the space-time quadrilateral side of a space-time hexahedron that is shared by the sliding layer by  $S_{sl}$ . There are now four different cuts for each space-time hexahedron in the sliding layer and four different cuts for each space-time hexahedron in the buffer layer:

1. In the sliding layer at  $t = t^n$  the quadrilateral is cut along the  $n_2^E - n_4^E$  diagonal while it is cut along the  $n_1^E - n_3^E$  diagonal at  $t = t^{n+1}$ , resulting in cuts 1 or 2 in fig. 7. Or, in the sliding layer at  $t = t^n$  the quadrilateral is cut along the  $n_1^E - n_3^E$  diagonal while it is cut along the  $n_2^E - n_4^E$  diagonal at  $t = t^{n+1}$ , resulting in cuts 5 or 6 in fig. 7.
2. In the buffer layer, the diagonal cut of  $S_{in}$  is the same as the diagonal cut of  $S_{sl}$ , resulting in cuts 3 or 4 in fig. 7. Or, in the buffer layer, the diagonal cut of  $S_{in}$  is opposite to the diagonal cut of  $S_{sl}$ , resulting in cuts 7 or 8 in fig. 7.

To obtain a conforming mesh we note that all diagonals of the space-time quadrilateral sides of a space-time hexahedron have to match with the diagonals of the space-time quadrilateral sides of an adjacent space-time hexahedron. Furthermore, the diagonals of the space-time quadrilateral sides of a space-time hexahedron have to match with the ‘chainsaw’ pattern of the outer boundary of the rotating space-time inner mesh and on the inner boundary the outer space-time static mesh. This results in four configurations of the  $2 \times 2$  block using the above eight cuts, see table 1. Consider, for example, the first configuration of table 1. Then, in the sliding layer, Cut 1 is adjacent to Cut 2. Cut 1 and Cut 2 are furthermore adjacent to Cuts 3 and 4, respectively, in the buffer layer. Configurations 2, 3, and 4 are defined similarly.

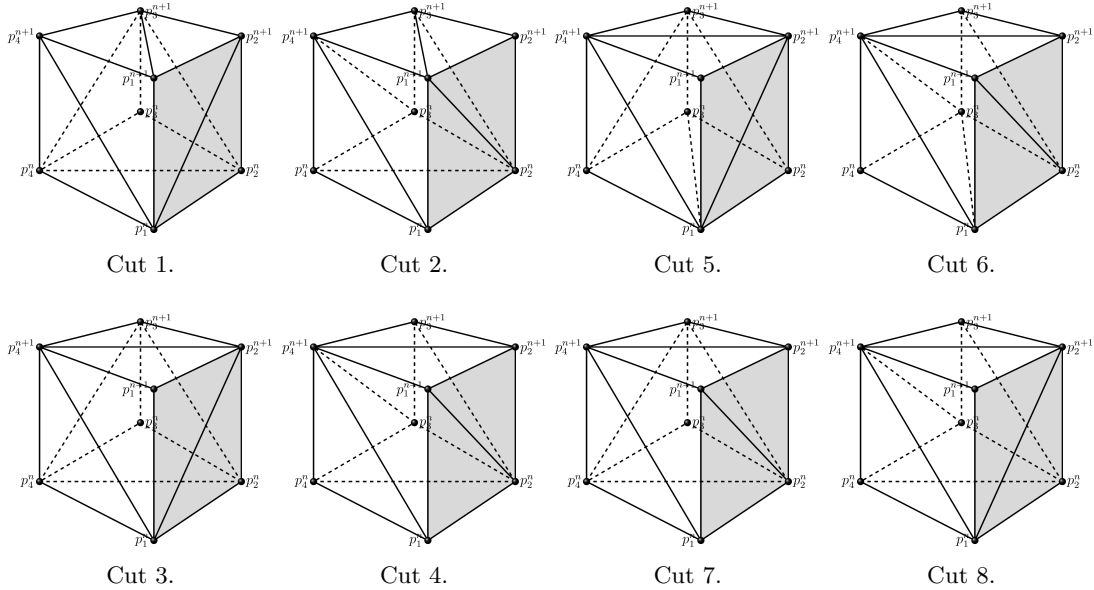


Figure 7: The gray shaded sides of the above hexahedra are the sides closest to the body. Top row: The four different cuttings of a hexahedron in the sliding layer when an edge swapping has taken place at  $t = t^{n+1}$ . Bottom row: The four different cuttings of a hexahedron in the buffer layer. There is no edge swapping in the buffer layer at  $t = t^{n+1}$ , but the diagonal in the quadrilateral side shared by the inner mesh (shaded gray) is either the same as the diagonal of the quadrilateral side shared by the sliding layer (cuts 3 and 4), or opposite (cuts 7 and 8).

## 5. Numerical examples

In this section we consider various test cases of increasing complexity and compare, where possible, our results to those found in the literature. For this we added the fluid-rigid body interaction and conforming sliding mesh technique algorithms to our space-time EHDG implementation of the Navier–Stokes equations as described previously in [22]. In particular, all simulations in this section have been implemented in the Modular Finite Element Method (MFEM) library [39]. We use the direct solver of MUMPS [40, 41] through PETSc [42, 43, 44] to solve the linear systems resulting from the Picard iteration eq. (12). Unless specified differently, we choose as tolerances for the Picard iteration eq. (13) and the rigid body stopping criterion eq. (17), respectively, as  $\delta_{\text{NS}} = 10^{-6}$  and  $\delta_{\text{rb}} = 10^{-5}$ . Finally, the penalty parameter  $\alpha$  in eq. (11) is chosen as  $\alpha = 6k^2$  where  $k$  is the polynomial degree used in eqs. (8) and (9) (see [45] for more information on the penalty parameter). In all simulations we take  $k = 2$ .

### 5.1. Vortex induced oscillations and galloping

In this example, we test the coupling algorithm between the fluid and the rigid body, but we do not yet consider the sliding mesh technique of section 4. To test this coupling we consider vertical galloping only, i.e., we only solve for the displacement  $d$  in eq. (6). We follow the setup of this test case as described previously in [1, 2, 35]. For this, consider a square object with sides of length 1 in a rectangular fluid domain with outer boundary sides of length 65 and 40. At time  $t = 0$  we place the center of the object at a distance of 20 from the left and bottom outer fluid domain boundary (see fig. 8).

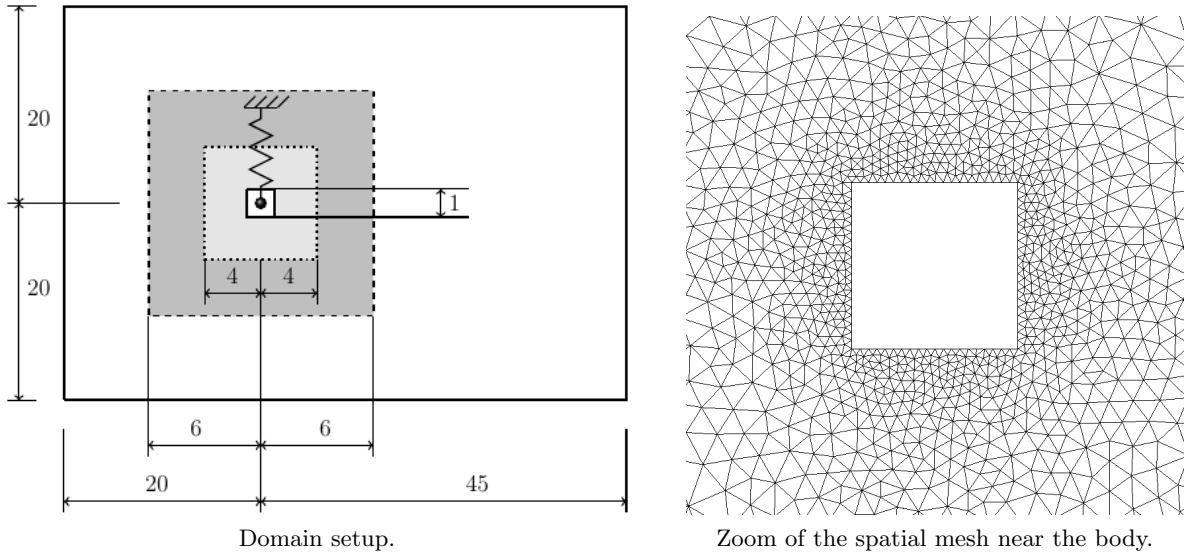


Figure 8: Left: depiction of the problem setup as described in section 5.1. Right: a zoom of the spatial mesh near the body.

The coefficients of the rigid-body spring-system are chosen as  $m = 20$ ,  $c_y = 0.00581195$ ,  $k_y = 3.08425$ . In the Navier–Stokes equations eq. (2) we choose the viscosity as  $\nu = 0.01$ , while the density in eq. (5) is chosen as  $\rho = 1$ . We impose  $\mathbf{u} = (2.5, 0)$  on the left outer boundary of the fluid domain, free-slip on the top and bottom outer boundaries, and a homogeneous Neumann boundary condition on the right outer boundary. The spatial mesh consists of 8510 triangles with 80 elements on the boundary of the body (see fig. 8 for a zoom of the mesh near the body). We set the time step equal to  $\Delta t = 0.1$ .

Since we consider the motion of a rigid body without rotation, we update our mesh in a similar manner as we used previously in [22, Section 5.4]: nodes inside the spatial box  $\Omega^{\text{in}}(t) = [-4, 4] \times [-4 + d(t), 4 + d(t)]$  (the light grey area in fig. 8) move with the body (the position of each node in  $\Omega^{\text{in}}(t)$  does not change with respect to the body); the movement of the nodes in  $\Omega^{\text{mid}}(t) = ([-6, 6] \times [-6, 6]) \setminus \Omega^{\text{in}}(t)$  (the dark grey area in fig. 8) decreases linearly with distance from the body; and the remaining nodes are fixed.

We plot the evolution of the amplitude of the motion of the rigid body in fig. 9 for  $t \in [0, 300]$ . We find a maximum amplitude of  $\max |y| = 1.3$  and a frequency of 0.62. Compared to results found in the literature, in which the maximum amplitude lies in the interval  $[1.08, 1.2]$  and the frequency lies in the interval  $[0.058, 0.069]$  (see, e.g., [1, 2, 35]), we note that we slightly over-predict the maximum amplitude, but that the frequency lies in the same range as other works. The velocity magnitude, at different evenly spaced points in time during two up-down periods, is shown in fig. 10.

## 5.2. Rotational galloping

In this section we combine the conforming sliding mesh technique described in section 4 with fluid-rigid body interaction by simulating the rotational galloping of a rectangle. The rotational galloping test case, in which there is no vertical motion, has also been considered in, for example, [1, 2].



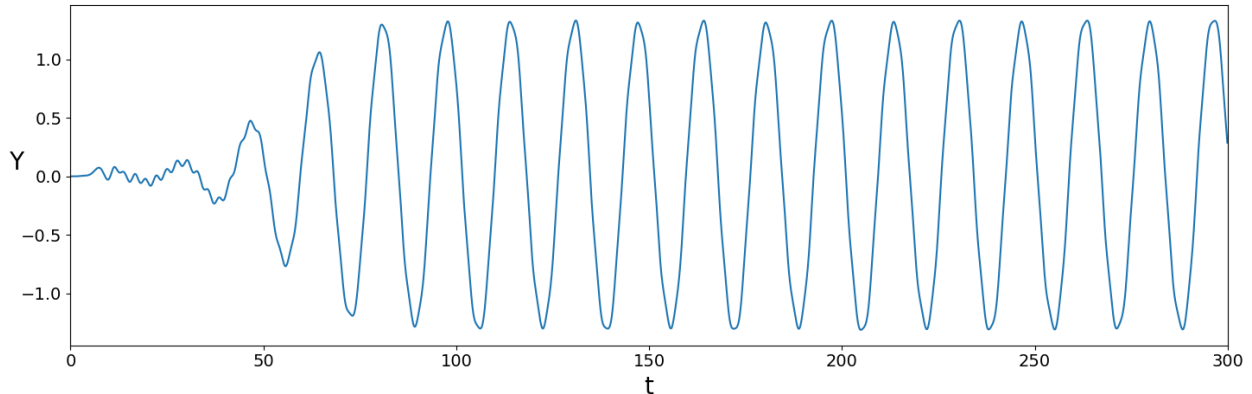


Figure 9: Evolution of the amplitude for the problem described in section 5.1

We consider a rectangular fluid domain of dimensions 52 by 60. The center of a rectangular rigid body, with dimensions 4 by 1, is placed at a distance 30 from the outer bottom wall of the fluid domain and a distance 12 from the outer left wall. See fig. 11 for a setup of the geometry. The coefficients of the rigid body spring system eq. (6b) are  $I_\theta = 400$ ,  $c_\theta = 78.54$ , and  $k_\theta = 61.685$ . For the fluid problem we again choose the viscosity and density as, respectively,  $\nu = 0.01$  and  $\rho = 1$ . We impose  $\mathbf{u} = (10, 0)$  on the left outer boundary of the fluid domain, free-slip on the top and bottom outer boundaries, and a homogeneous Neumann boundary condition on the right outer boundary. We set the time step equal to  $\Delta t = 0.15$ .

In this simulation we compute results on a coarse mesh, consisting of 6030 triangles with 116 elements on the boundary of the body, and on a fine mesh with 13 722 triangles with 168 body boundary elements (see fig. 12 for a zoom of the mesh near the body). The inner and outer radii of the annulus consisting of the sliding and buffer layer are placed at a distance of, respectively, 4.4 and 5 from the center of the rigid body. This annulus is initially (before creating the space-time tetrahedral mesh) tessellated into 100 quadrilaterals for the coarse mesh and 152 for the fine mesh.

The evolution of the rotational angle for  $t \in [0, 300]$  is shown in fig. 13. On the coarse mesh we find a maximum amplitude of  $\max |y| = 0.286$  and a frequency of 0.048. On the fine mesh we find a maximum amplitude of  $\max |y| = 0.285$  and a frequency of 0.049. These results compare well to results found in the literature. Indeed, [1, 2, 35] predict the maximum amplitude to lie in the interval  $[0.223, 0.283]$  and the frequency to lie in the interval  $[0.048, 0.052]$ .

A plot of the fine mesh at maximum, zero, and minimum angle of the body is given in fig. 14. Observe that the connectivity changes only in the sliding layer. Finally, we plot in fig. 15 the velocity magnitude computed on the fine mesh at different, evenly spaced, points in time during one period.

### 5.3. H-shaped bridge

We now consider the fluttering H-shaped bridge example of [2, Section 8.4]. In particular, we consider a fluid-rigid body interaction simulation in which both rotational and vertical displacement of the body are computed for.

The setup of the geometry is depicted in fig. 16. The coefficients of the rigid body spring system eq. (6) are chosen as  $I_\theta = 25\,300$ ,  $c_\theta = 0$ ,  $k_\theta = 40\,000$ ,  $m = 3000$ ,  $c_y = 0$ , and  $k_y = 2000$ . For

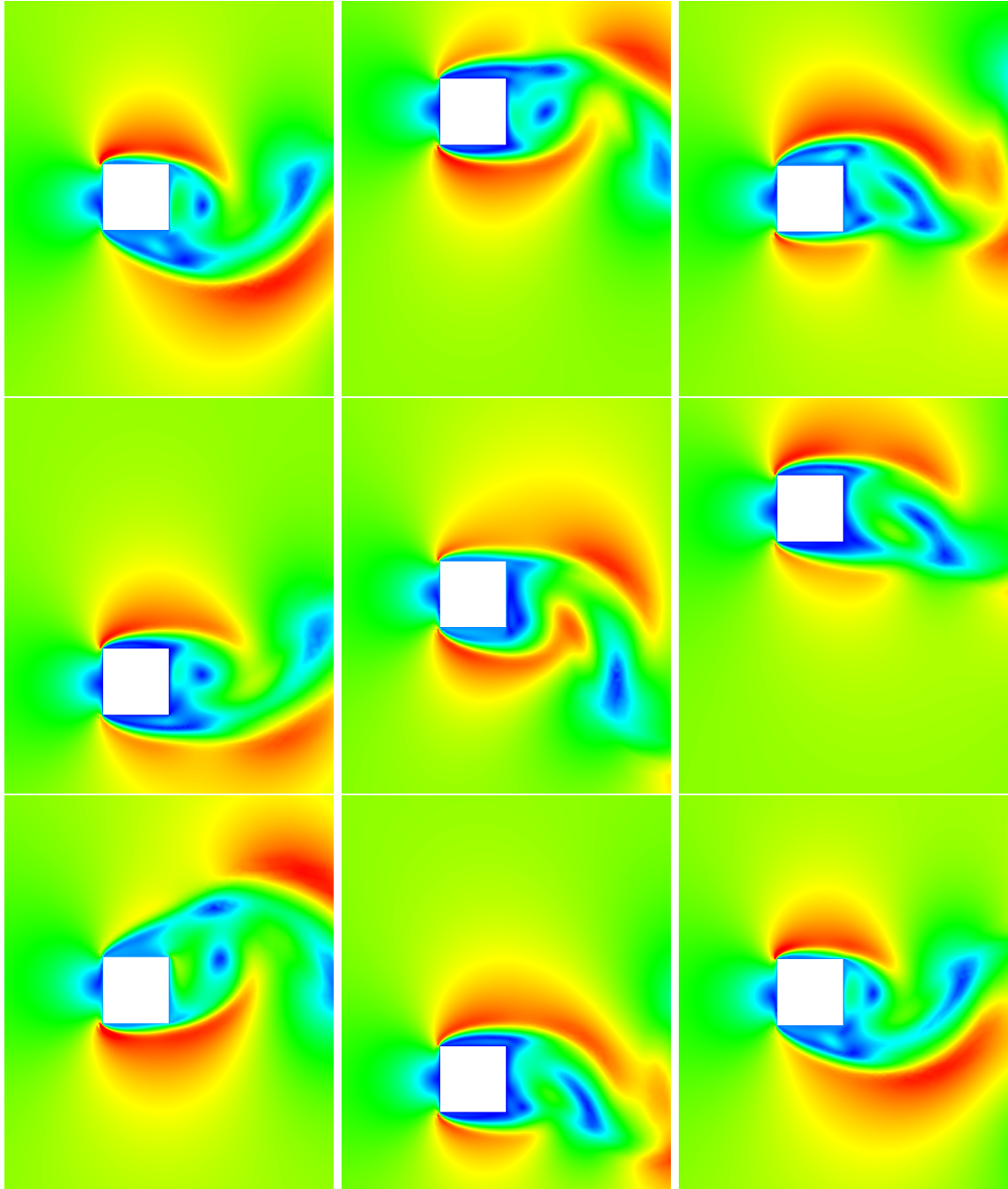


Figure 10: The velocity magnitude at different, evenly spaced, points in time during two up-down periods for the problem described in section 5.1.

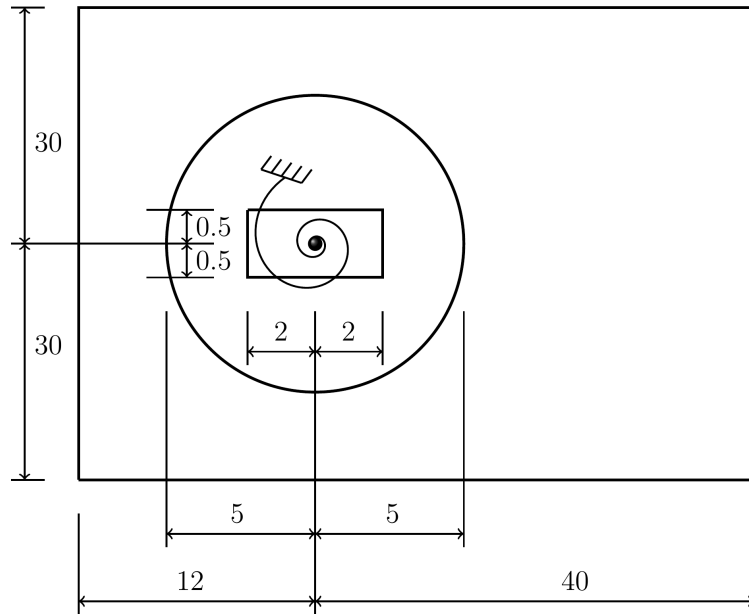


Figure 11: Set up of the problem of section 5.2.

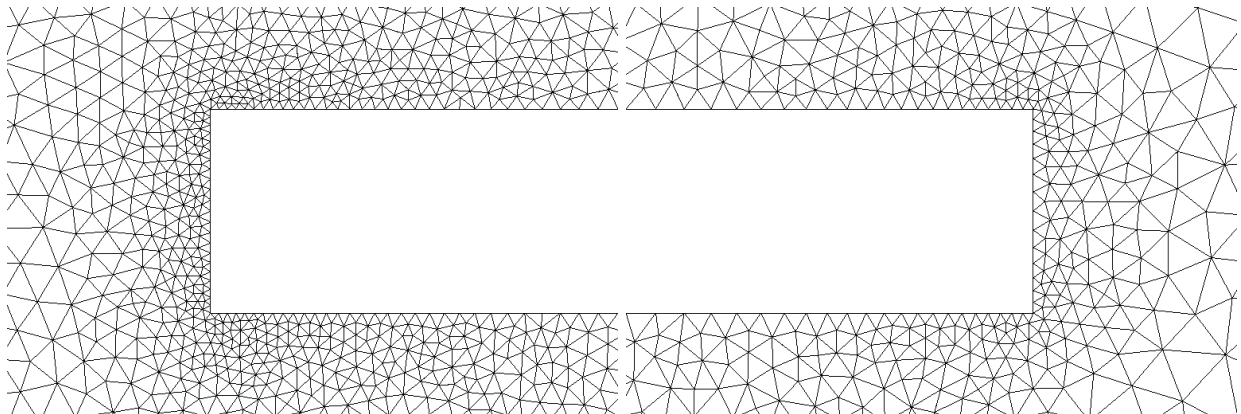


Figure 12: Fine (left) and coarse (right) mesh near the body for the problem described in section 5.2.

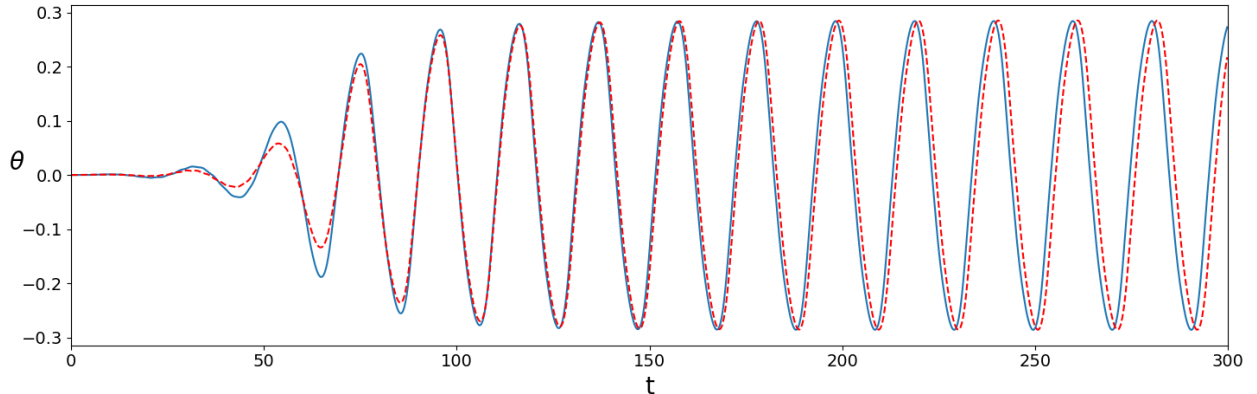


Figure 13: Evolution of the rotational angle computed on the coarse mesh (blue) and the fine mesh (red). See section 5.2.

the fluid problem we choose  $\nu = 0.1$  and  $\rho = 1.25$ . We impose  $\mathbf{u} = (10, 0)$  on the left boundary, free-slip on the top and the bottom boundaries, and a homogeneous Neumann boundary condition on the right boundary. As time step we choose  $\Delta t = 0.05$ .

We again consider two different meshes: a coarse mesh containing 5901 triangles with 156 body boundary elements and a fine mesh containing 12 163 triangles with 272 body boundary elements (see fig. 17 for a zoom of the mesh near the body). We place the inner and outer radii of the annulus consisting of the sliding and buffer layer at a distance of, respectively, 14 and 15 from the center of the H-shaped bridge. This annulus is initially partitioned into 100 quadrilaterals when computing on the coarse mesh and 152 when computing on the fine mesh.

The vertical displacement is handled similarly as in section 5.1. The nodes inside the spatial box  $\Omega^{\text{in}}(t) = [-16, 16] \times [-16 + d(t), 16 + d(t)]$  move vertically with the body; the vertical movement of the nodes in  $\Omega^{\text{mid}}(t) = ([-20, 20] \times [-20, 20]) \setminus \Omega^{\text{in}}(t)$  decreases linearly with distance from  $\Omega^{\text{in}}$ ; and the remaining nodes are fixed. Note that the rotating and sliding meshes are completely contained in  $\Omega^{\text{in}}(t)$ .

We plot, for  $t \in [0, 250]$ , the evolution of the vertical displacement and the rotational angle of the rigid body in fig. 18. We observe that the oscillations develop into a stable time-periodic pattern at approximately  $t = 190$ . For  $t > 190$  we find  $\max |y| = 0.74$ . For  $t > 190$  we also observe that  $\max |\theta| = 0.925$  when computed on the coarse mesh and  $\max |\theta| = 0.935$  when computed on the fine mesh. The frequency of both the displacement and the rotation is 0.185. These results compare well with [2], in which  $\max |y| \in [0.75, 0.85]$ ,  $\max |\theta| \in [0.9, 1]$ , and the frequency is 0.186. To conclude this section, we plot the velocity magnitude at different, evenly spaced, points in time during a full period ( $t > 190$ ) in fig. 19.

#### 5.4. Rotating turbine

In this final test case, we consider a model turbine simulation inspired by [3, Section 10.1]. We refer to fig. 20 for the setup of the geometry. For this example we set  $I_\theta = 1.5$ ,  $c_\theta = k_\theta = 0$  in eq. (6b) (note that we do not have vertical motion in this example) and choose  $\nu = 0.1$  and  $\rho = 1$  for the fluid problem. We impose  $\mathbf{u} = (1250(1.25 - y)(y - 0.85), 0)$  on the left inflow boundary,  $\mathbf{u} = \mathbf{0}$  on the walls, and a homogeneous Neumann boundary condition on the bottom right outflow

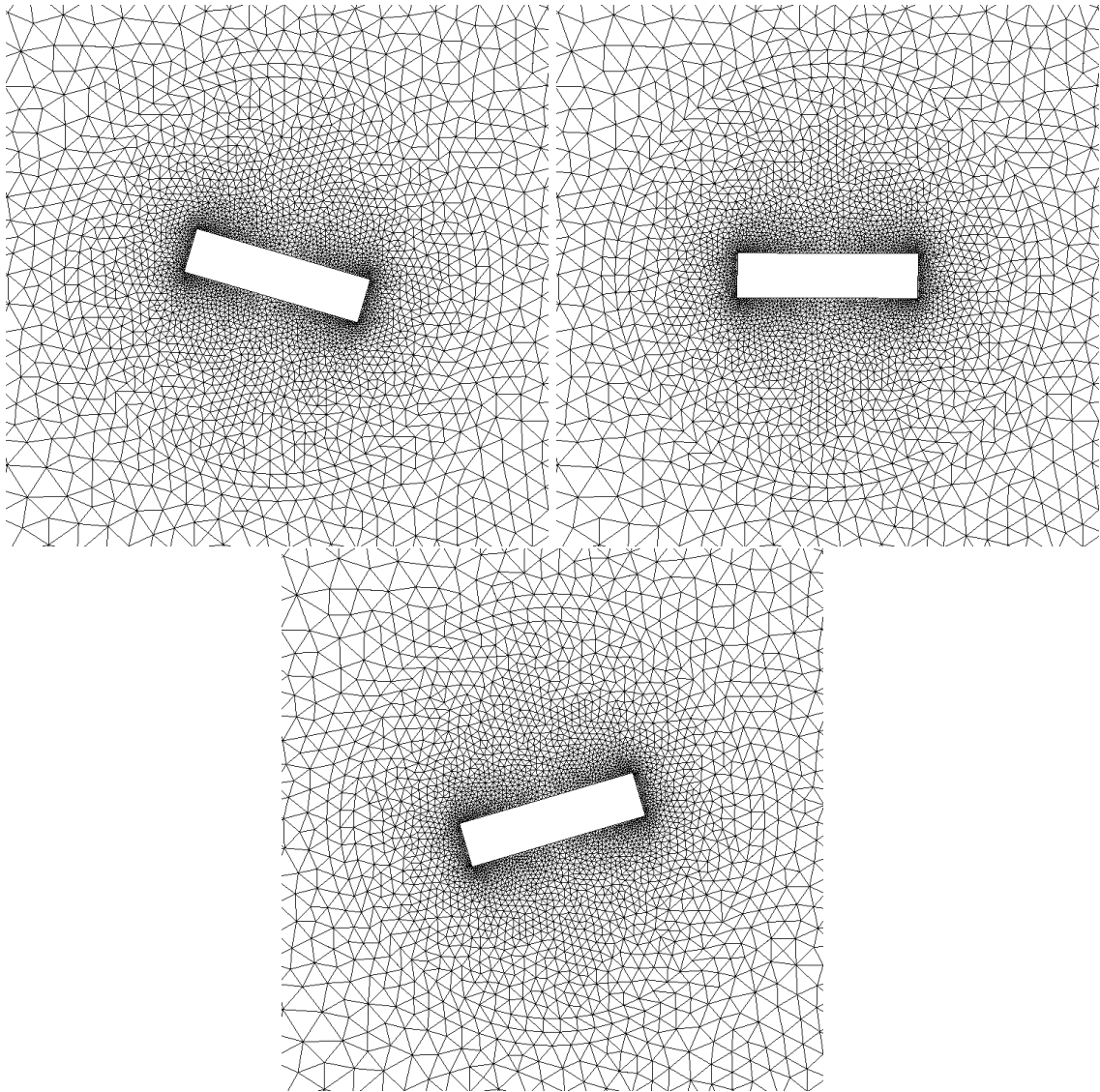


Figure 14: The mesh at the maximum, zero, and minimum angle of the body for the problem described in section 5.2.

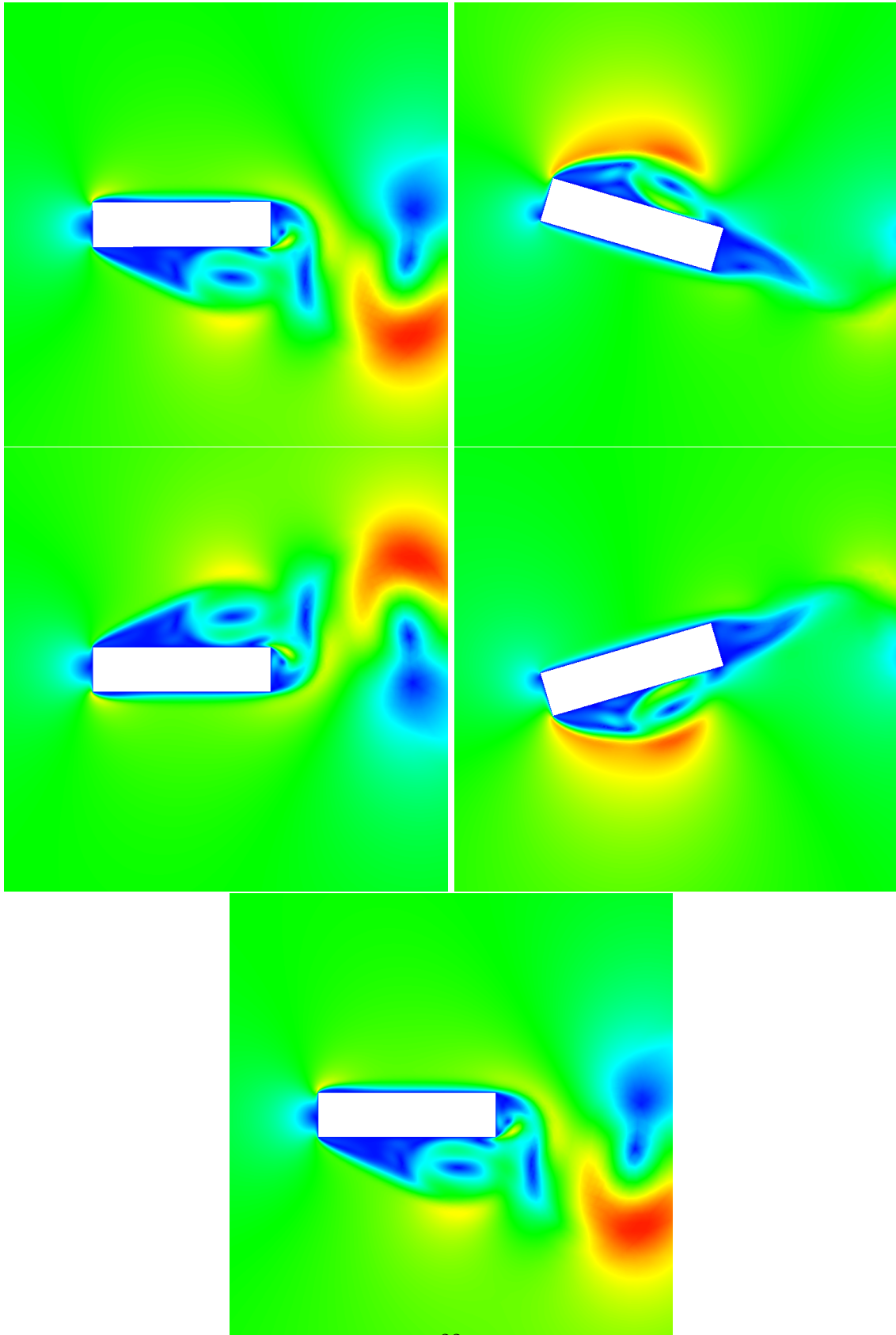


Figure 15: The velocity magnitude computed on the fine mesh at different, evenly spaced, points in time during one period for the problem described in section 5.2.

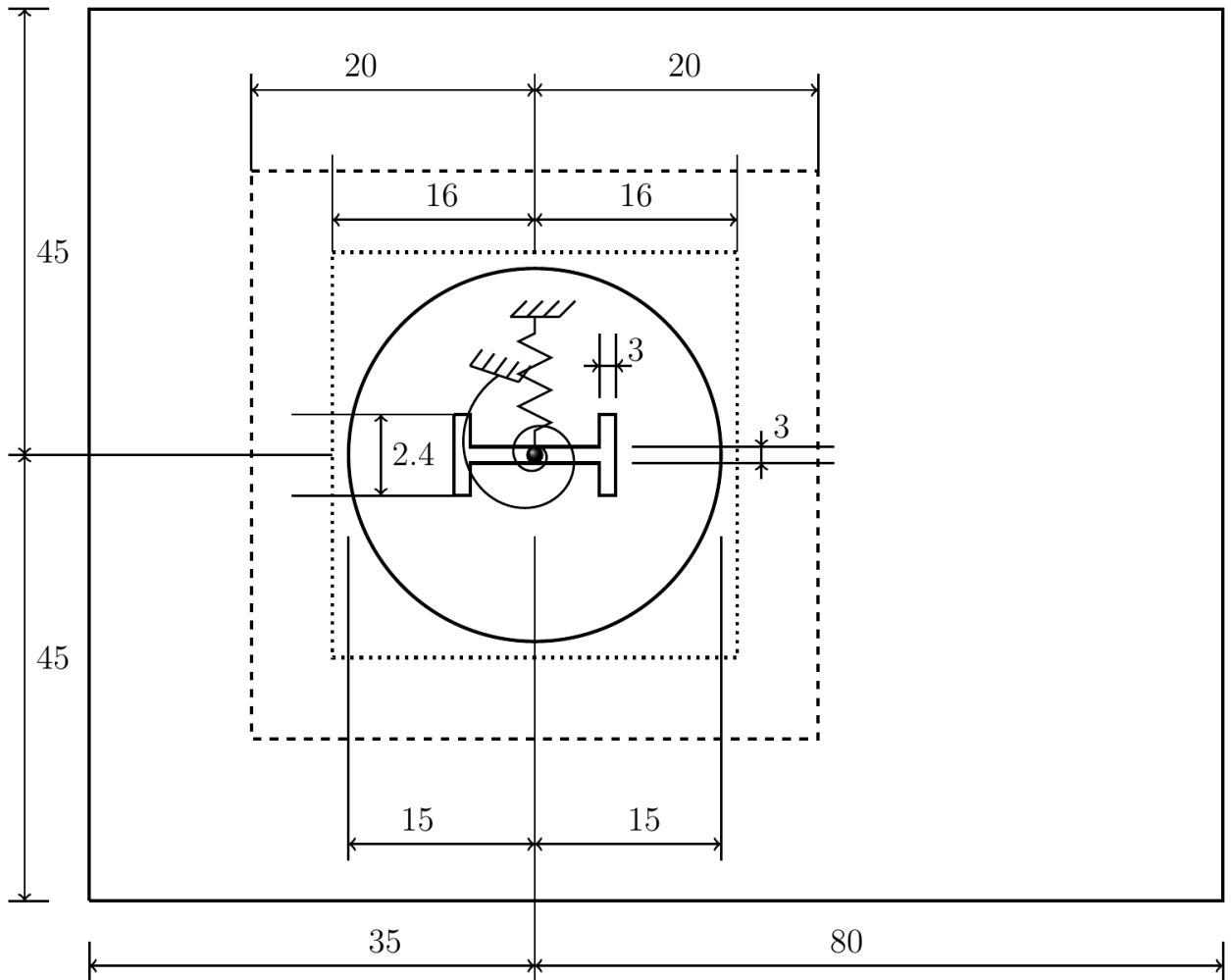


Figure 16: Set up of the fluttering H-shaped bridge example of section 5.3.

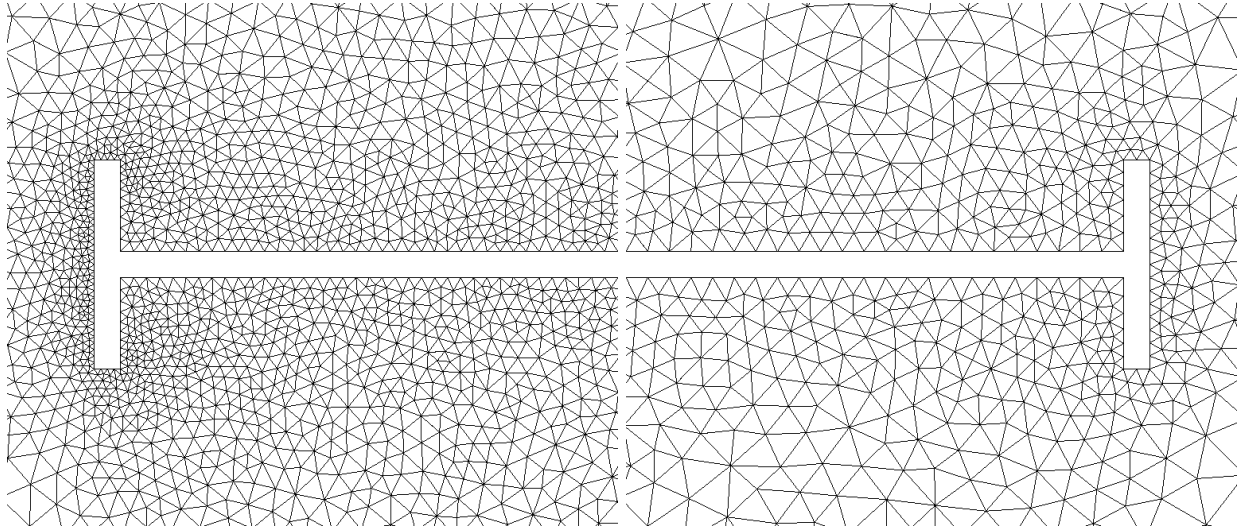


Figure 17: A zoom of the mesh near the body for the problem described in section 5.3. Left: fine mesh. Right: coarse mesh.

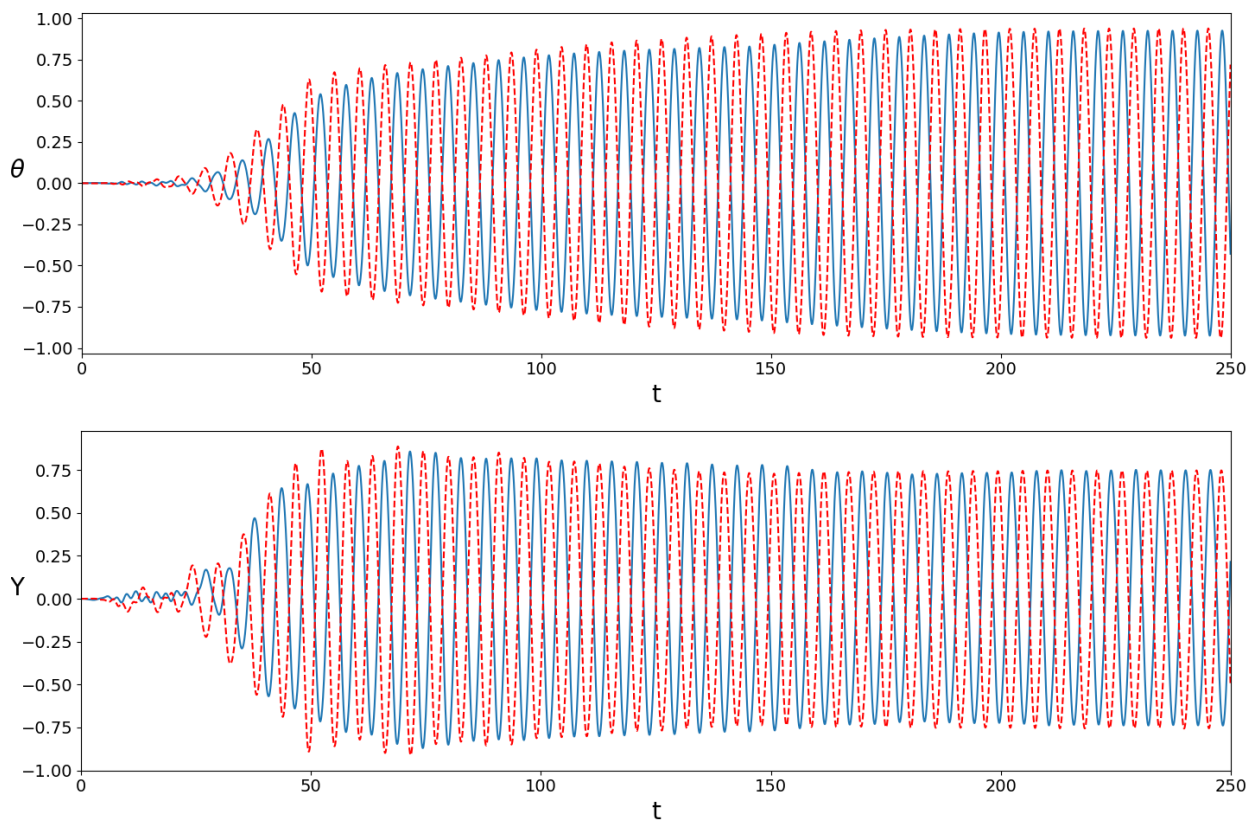


Figure 18: Evolution of the rotational angle (top) and vertical displacement (bottom) computed on the coarse mesh (blue) and the fine mesh (red). See section 5.3 for more details.



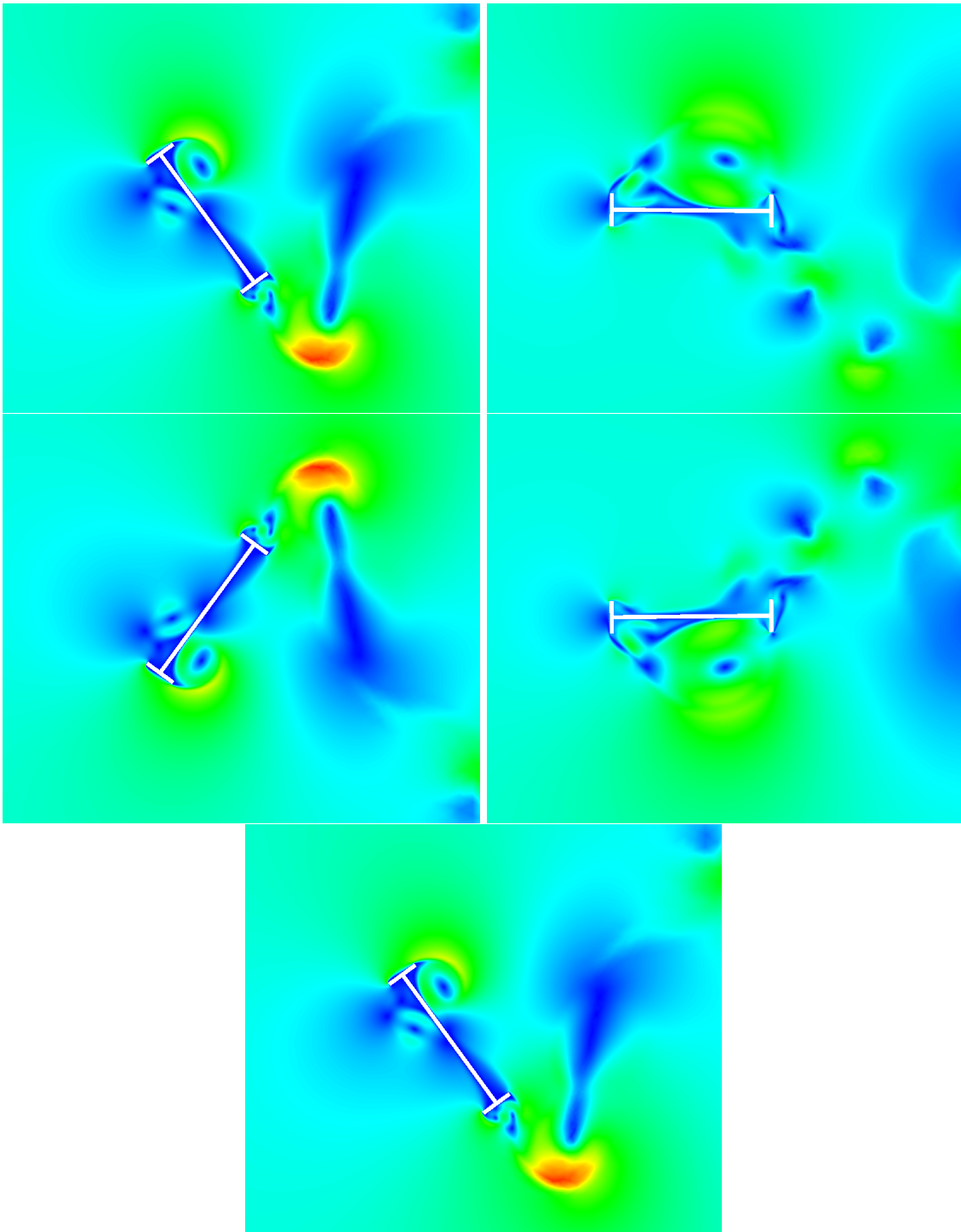


Figure 19: The velocity magnitude at different, evenly spaced, points in time during a full period ( $t > 190$ ) for the problem described in section 5.3.

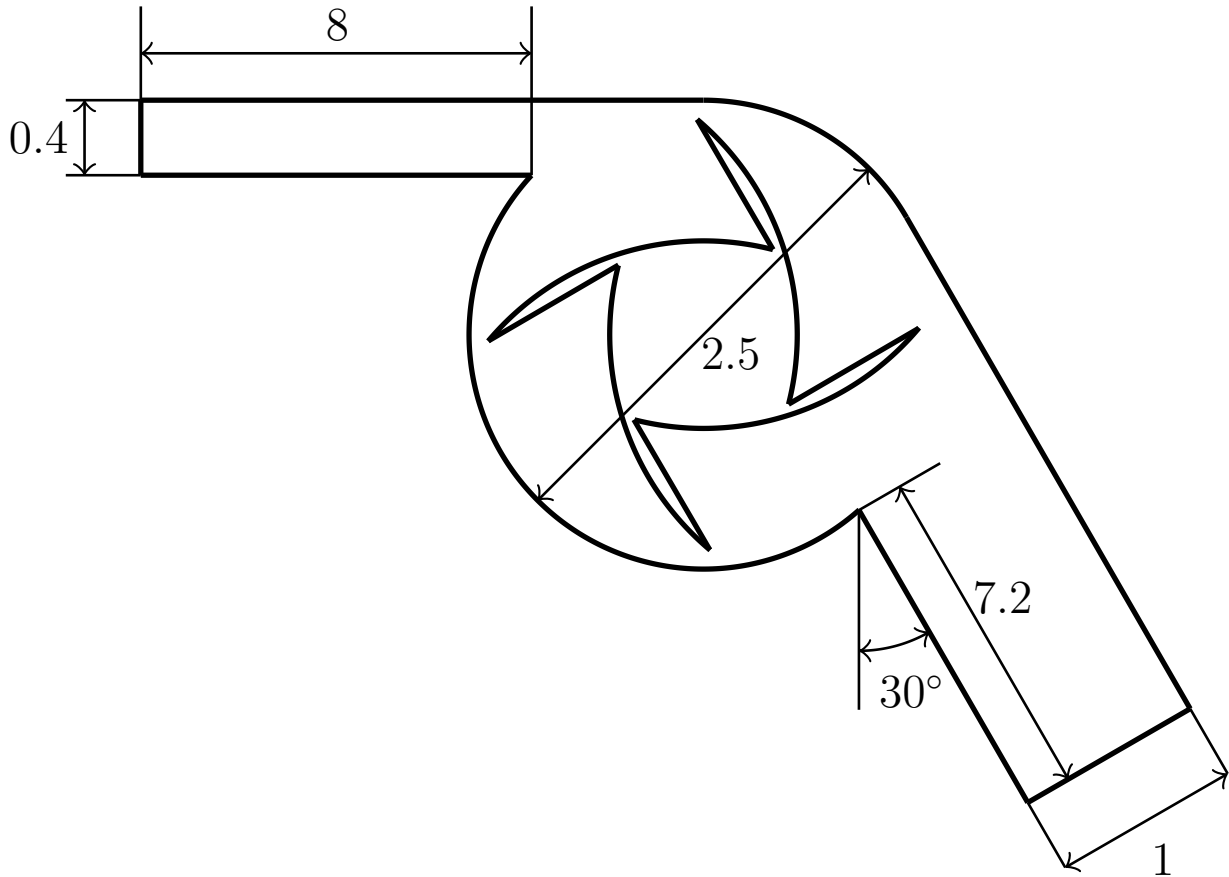


Figure 20: Set up of the geometry of the rotating turbine example of section 5.4.

boundary. As time step we choose  $\Delta t = 0.001$ . For this test we choose  $\delta_{NS} = 10^{-5}$  in eq. (13) and  $\delta_{rb} = 10^{-4}$  in eq. (17).

In fig. 21 we plot the evolution of the rotational angle and the angular velocity of the turbine for  $t \in [0, 1.75]$ . We observe that the rotational velocity increases until  $t = 0.5$  and then slightly oscillates around  $\dot{\theta} = 35$ . We furthermore observe from fig. 21 that the turbine completes multiple full rotations throughout the simulation. We show the mesh at different, evenly spaced, points in time during half a rotation ( $t > 0.5$ ) in fig. 22. Finally, we plot the velocity magnitude on these meshes in fig. 23.

## 6. Conclusions

In this paper we presented an exactly mass conserving space-time embedded-hybridizable discontinuous Galerkin finite element discretization for fluid-rigid body interaction problems. Furthermore, we introduced a conforming sliding mesh technique, using edge swapping, for simulations where the rotational motion of the rigid body is large. By noting that our edge swapping algorithm results in one of only four different mesh connectivity sets, and that each of these sets can be

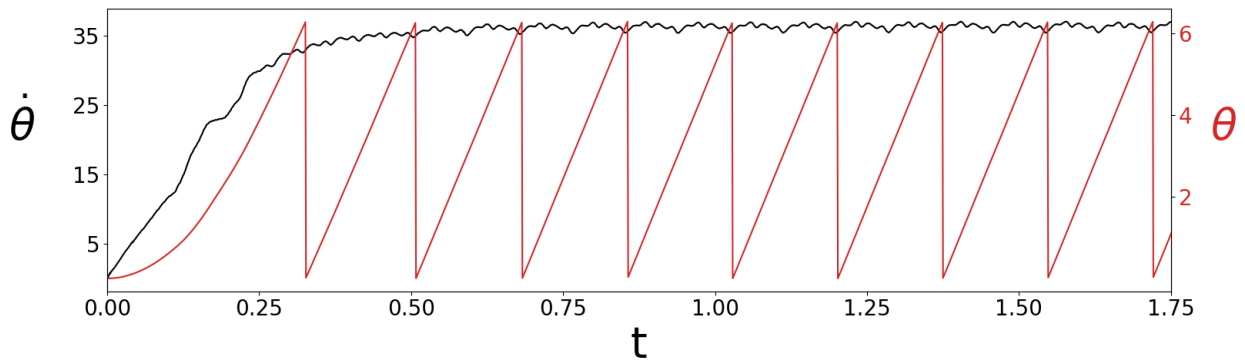


Figure 21: Evolution of the angular velocity  $\dot{\theta}$  and rotational angle  $\theta$  for the rotating turbine problem (section 5.4).

determined before the start of a simulation, additional computational cost due to edge swapping is kept low.

#### Acknowledgements

TH would like to thank Oakland University for the URC Faculty Research Fellowship Award. SR gratefully acknowledges support from the Natural Sciences and Engineering Research Council of Canada through the Discovery Grant program (RGPIN-05606-2015).

#### References

- [1] I. Robertson, L. Li, S. J. Sherwin, P. W. Bearman, A numerical study of rotational and transverse galloping rectangular bodies, *J. Fluid. Struct* 17 (2003) 681–699. doi:[10.1016/S0889-9746\(03\)00008-2](https://doi.org/10.1016/S0889-9746(03)00008-2).
- [2] W. Dettmer, D. Perić, A computational framework for fluid-rigid body interaction: finite element formulation and applications, *Comput. Methods. Appl. Mech. Engrg.* 195 (2006) 1633–1666. doi:[10.1016/j.cma.2005.05.033](https://doi.org/10.1016/j.cma.2005.05.033).
- [3] P. H. Saksono, W. G. Dettmer, D. Perić, An adaptive remeshing strategy for flows with moving boundaries and fluid-structure interaction, *Int. J. Numer. Meth. Eng.* 71 (2007) 1009–1050. doi:[10.1002/nme.1971](https://doi.org/10.1002/nme.1971).
- [4] S. Čanić, Moving boundary problems, *B. Am. Math. Soc.* 58 (2021) 79–106. doi:[10.1090/bull/1703](https://doi.org/10.1090/bull/1703).
- [5] M. Bukač, S. Čanić, R. Glowinski, J. Tambača, A. Quaini, Fluid-structure interaction in blood flow capturing non-zero longitudinal structure displacement, *J. Comput. Phys.* 235 (2013) 515–541. doi:[10.1016/j.jcp.2012.08.033](https://doi.org/10.1016/j.jcp.2012.08.033).
- [6] M. Bukač, S. Čanić, J. Tambača, Y. Wang, Fluid-structure interaction between pulsatile blood flow and a curved stented coronary artery on a beating heart: a four stent computational study, *Comput. Methods. Appl. Mech. Engrg.* 350 (2019) 679–700. doi:[10.1016/j.cma.2019.03.034](https://doi.org/10.1016/j.cma.2019.03.034).
- [7] M. Neunteufel, J. Schöberl, Fluid-structure interaction with H(div)-conforming finite elements, *Comput. Struct.* 243 (2021) 106402. doi:[10.1016/j.compstruc.2020.106402](https://doi.org/10.1016/j.compstruc.2020.106402).
- [8] G. Fu, W. Kuang, A monolithic divergence-conforming HDG scheme for a linear fluid-structure interaction model, arXiv preprint arXiv:2012.00128 (2020).
- [9] R. J. Labeur, G. N. Wells, Interface stabilised finite element method for moving domains and free surface flows, *Comput. Methods Appl. Mech. Engrg.* 198 (2009) 615–630. doi:[10.1016/j.cma.2008.09.014](https://doi.org/10.1016/j.cma.2008.09.014).
- [10] G. Hauke, T. J. R. Hughes, A unified approach to compressible and incompressible flows, *Comput. Methods. Appl. Mech. Engrg.* 113 (1994) 389–395. doi:[10.1016/0045-7825\(94\)90055-8](https://doi.org/10.1016/0045-7825(94)90055-8).
- [11] A. A. Johnson, T. E. Tezduyar, Mesh update strategies in parallel finite element computations of flow problems with moving boundaries and interfaces, *Comput. Methods. Appl. Mech. Engrg.* 119 (1994) 73–94. doi:[10.1016/0045-7825\(94\)00077-8](https://doi.org/10.1016/0045-7825(94)00077-8).
- [12] D. N’dri, A. Garon, A. Fortin, A new stable space-time formulation for two-dimensional and three-dimensional incompressible viscous flow, *Int. J. Numer. Meth. Fluids* 37 (2001) 865–884. doi:[10.1002/flid.174](https://doi.org/10.1002/flid.174).

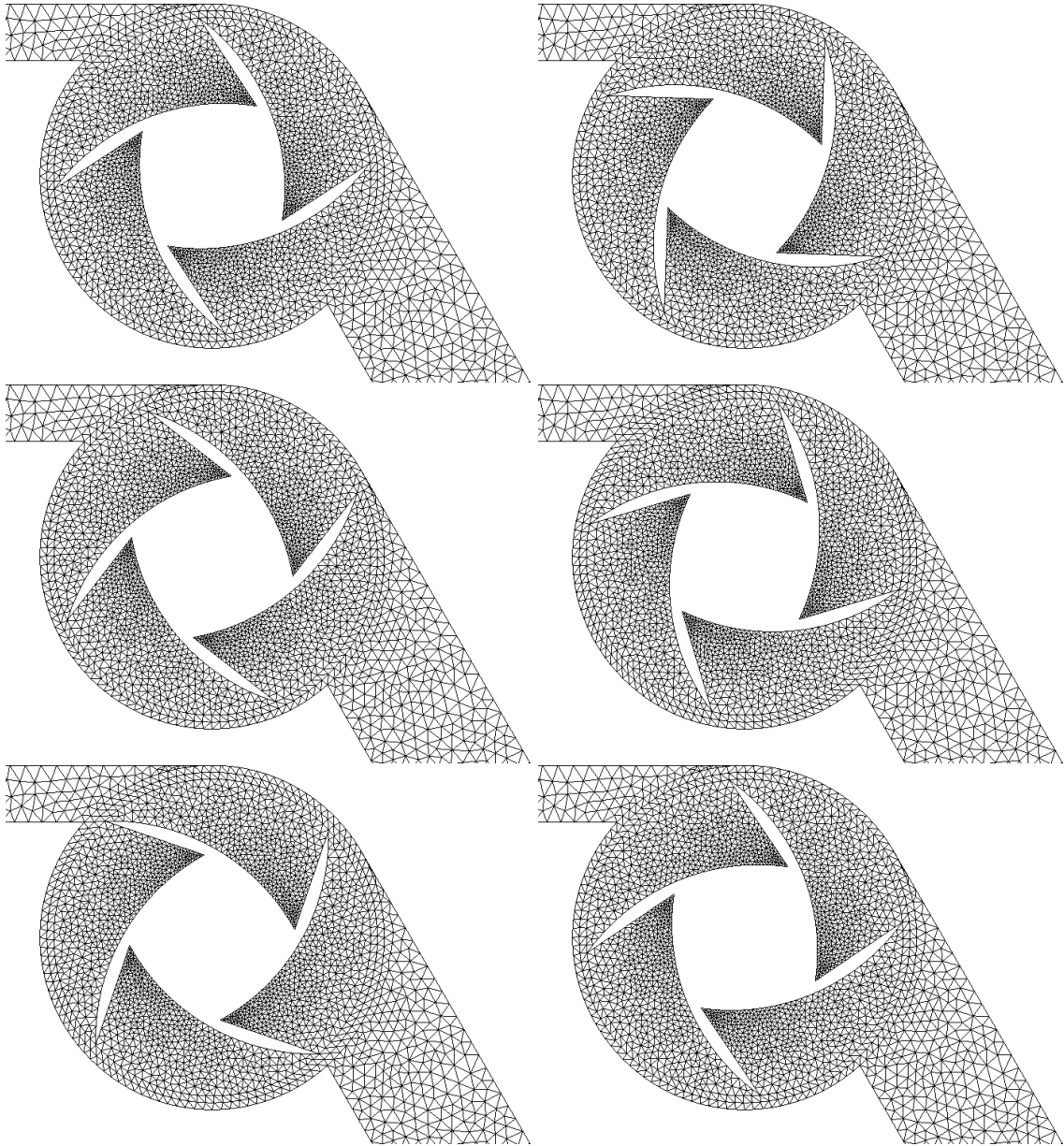


Figure 22: The meshes at different, evenly spaced, points in time during half a rotation of the turbine for the problem described in section 5.4.

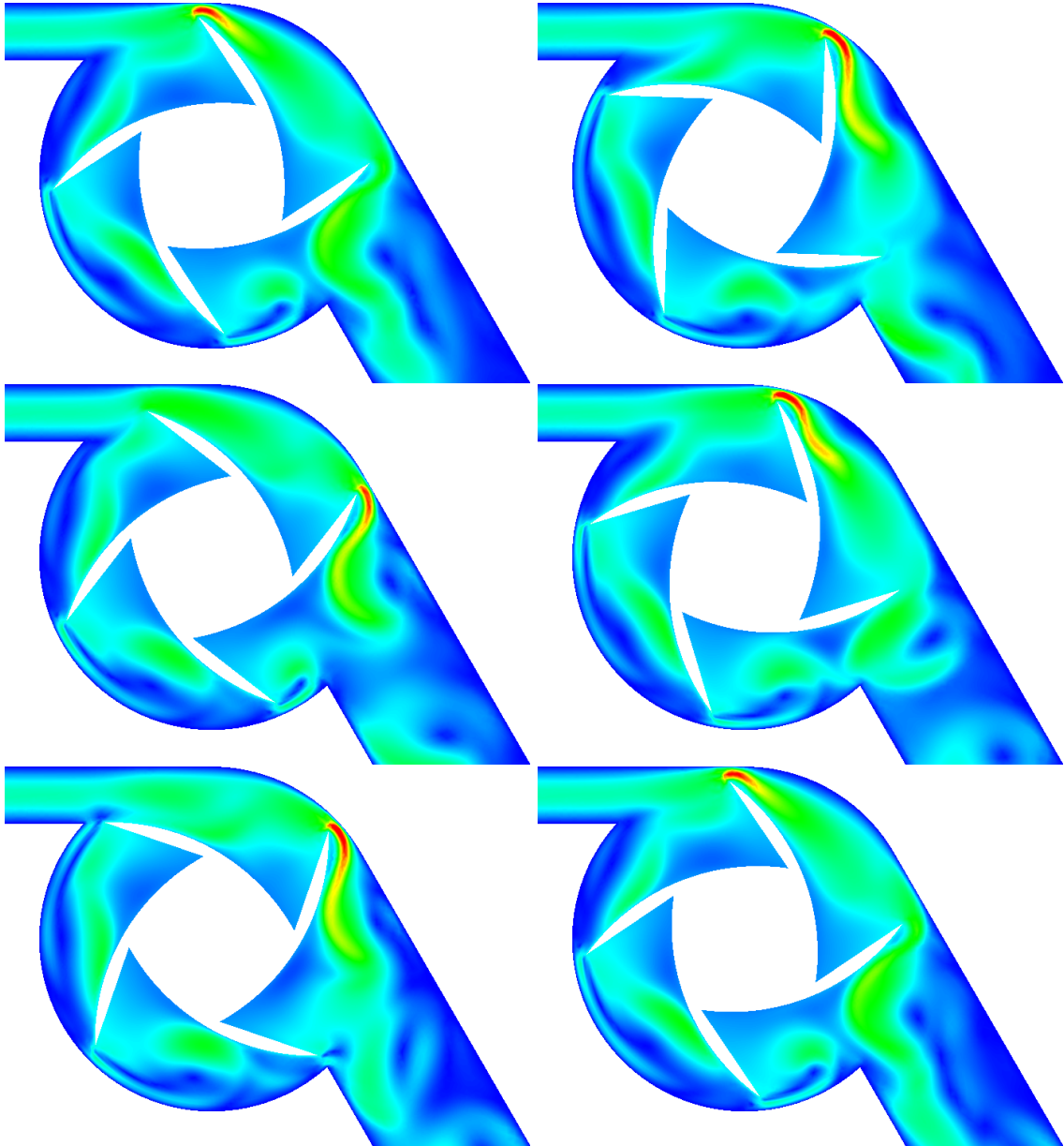


Figure 23: The velocity magnitude computed on the meshes of fig. 22.

- [13] D. N’dri, A. Garon, A. Fortin, Incompressible Navier–Stokes computations with stable and stabilized space-time formulations: a comparative study, *Commun. Numer. Meth. Engng.* 18 (2002) 495–512. doi:[10.1002/cnm.507](https://doi.org/10.1002/cnm.507).
- [14] S. Rhebergen, B. Cockburn, J. van der Vegt, A space-time discontinuous Galerkin method for the incompressible Navier–Stokes equations, *J. Comput. Phys.* 233 (2013) 339–358. doi:[10.1016/j.jcp.2012.08.052](https://doi.org/10.1016/j.jcp.2012.08.052).
- [15] M. Tavelli, M. Dumbser, A staggered space-time discontinuous Galerkin method for the incompressible Navier–Stokes equations on two-dimensional triangular meshes, *Comput. Fluids* 119 (2015) 235–249. doi:[10.1016/j.compfluid.2015.07.003](https://doi.org/10.1016/j.compfluid.2015.07.003).
- [16] M. Tavelli, M. Dumbser, A staggered space-time discontinuous Galerkin method for the three-dimensional incompressible Navier–Stokes equations on unstructured tetrahedral meshes, *J. Comput. Phys.* 319 (2016) 294–323. doi:[10.1016/j.jcp.2016.05.009](https://doi.org/10.1016/j.jcp.2016.05.009).
- [17] J. van der Vegt, J. Sudirham, A space-time discontinuous Galerkin method for the time-dependent Oseen equations, *Appl. Numer. Math* 58 (2008) 1892–1917. doi:[10.1016/j.apnum.2007.11.010](https://doi.org/10.1016/j.apnum.2007.11.010).
- [18] T. E. Tezduyar, M. Behr, J. Liou, A new strategy for finite element computations involving moving boundaries and interfaces—the DSD/ST procedure: I. The concept and the preliminary numerical tests, *Comput. Methods. Appl. Mech. Engng.* 94 (1992) 339–351. doi:[10.1016/0045-7825\(92\)90059-S](https://doi.org/10.1016/0045-7825(92)90059-S).
- [19] T. E. Tezduyar, M. Behr, S. Mittal, J. Liou, A new strategy for finite element computations involving moving boundaries and interfaces—The deforming-spatial-domain/space-time procedure: II. Computation of free-surface flows, two-liquid flows, and flows with drifting cylinders, *Comput. Methods. Appl. Mech. Engng.* 94 (1992) 353–371. doi:[10.1016/0045-7825\(92\)90060-W](https://doi.org/10.1016/0045-7825(92)90060-W).
- [20] T. E. Tezduyar, S. Sathe, R. Keedy, K. Stein, Space-time finite element techniques for computation of fluid-structure interactions, *Comput. Methods Appl. Mech. Engng.* 195 (2006) 2002–2027. doi:[10.1016/j.cma.2004.09.014](https://doi.org/10.1016/j.cma.2004.09.014).
- [21] B. Hübner, E. Walhorn, D. Dinkler, A monolithic approach to fluid-structure interaction using space-time finite elements, *Comput. Methods Appl. Mech. Engng.* 193 (2004) 2087–2104. doi:[10.1016/j.cma.2004.01.024](https://doi.org/10.1016/j.cma.2004.01.024).
- [22] T. L. Horvath, S. Rhebergen, An exactly mass conserving space-time embedded-hybridized discontinuous Galerkin method for the Navier–Stokes equations on moving domains, *J. Comput. Phys.* 417 (2020). doi:[10.1016/j.jcp.2020.109577](https://doi.org/10.1016/j.jcp.2020.109577).
- [23] S. Rhebergen, G. N. Wells, Analysis of a hybridized/interface stabilized finite element method for the Stokes equations, *SIAM J. Numer. Anal.* 55 (2017) 1982–2003. doi:[10.1137/16M1083839](https://doi.org/10.1137/16M1083839).
- [24] S. Rhebergen, G. N. Wells, A hybridizable discontinuous Galerkin method for the Navier–Stokes equations with pointwise divergence-free velocity field, *J. Sci. Comput.* 76 (2018) 1484–1501. doi:[10.1007/s10915-018-0671-4](https://doi.org/10.1007/s10915-018-0671-4).
- [25] S. Rhebergen, G. N. Wells, An embedded-hybridized discontinuous Galerkin finite element method for the Stokes equations, *Comput. Methods Appl. Mech. Engng.* 367 (2020). doi:[10.1016/j.cam.2019.112476](https://doi.org/10.1016/j.cam.2019.112476).
- [26] T. L. Horvath, S. Rhebergen, A locally conservative and energy-stable finite element method for the Navier–Stokes problem on time-dependent domains, *Int. J. Numer. Meth. Fluids* 89 (2019) 519–532. doi:[10.1002/flid.4707](https://doi.org/10.1002/flid.4707).
- [27] K. L. A. Kirk, T. L. Horvath, S. Rhebergen, Analysis of an exactly mass conserving space-time hybridized discontinuous Galerkin method for the time-dependent Navier–Stokes equations, arXiv preprint arXiv:2103.13492 (2021).
- [28] B. Cockburn, J. Gopalakrishnan, R. Lazarov, Unified hybridization of discontinuous Galerkin, mixed, and continuous Galerkin methods for second order elliptic problems, *SIAM J. Numer. Anal.* 47 (2009) 1319–1365. doi:[10.1137/070706616](https://doi.org/10.1137/070706616).
- [29] E. Ferrer, R. H. J. Willden, A high order discontinuous Galerkin – Fourier incompressible 3D Navier–Stokes solver with rotating sliding meshes, *J. Comput. Phys.* 231 (2012) 7037–7056. doi:[10.1016/j.jcp.2012.04.039](https://doi.org/10.1016/j.jcp.2012.04.039).
- [30] J. A. Cottrell, T. J. R. Hughes, Y. Bazilevs, *Isogeometric Analysis: Toward Integration of CAD and FEA*, Wiley, New York, 2009.
- [31] G. Anagnostou, Nonconforming sliding spectral element methods for the unsteady incompressible Navier–Stokes equations, Ph.D. thesis, Massachusetts Institute of Technology, 1990.
- [32] L. Wang, P.-O. Persson, A high-order discontinuous Galerkin method with unstructured space-time meshes for two-dimensional compressible flows on domains with large deformations, *Comput. Fluids* 118 (2015) 53–68. doi:[10.1016/j.compfluid.2015.05.026](https://doi.org/10.1016/j.compfluid.2015.05.026).
- [33] R. Calderer, A. Masud, A multiscale stabilized ALE formulation for incompressible flows with moving boundaries, *Comput. Mech.* 46 (2010) 185–197. doi:[10.1007/s00466-010-0487-z](https://doi.org/10.1007/s00466-010-0487-z).
- [34] C. Farhat, K. G. V. der Zee, P. Geuzaine, Provably second-order time-accurate loosely-coupled solution algorithms for transient nonlinear computational aeroelasticity, *Comput. Methods Appl. Mech. Engng.* 195 (2006) 1973–2001. doi:[10.1016/j.cma.2004.11.031](https://doi.org/10.1016/j.cma.2004.11.031).

- [35] C. Kadapa, W. G. Dettmer, D. Perić, A stabilised immersed boundary method on hierarchical b-spline grids for fluid-rigid body interaction with solid-solid contact, *Comput. Methods Appl. Mech. Engrg.* 318 (2017) 242–269. doi:[10.1016/j.cma.2017.01.024](https://doi.org/10.1016/j.cma.2017.01.024).
- [36] S. Rugonyi, K. J. Bathe, On finite element analysis of fluid flows fully coupled with structural interactions, *CMES Comput. Model. Eng. Sci.* 2 (2001) 195–212. doi:[10.3970/cmesci.2001.002.195](https://doi.org/10.3970/cmesci.2001.002.195).
- [37] T. E. Tezduyar, S. Sathe, Modelling of fluid-structure interactions with the space-time finite elements: Solution techniques, *Int. J. Numer. Meth. Fl.* 54 (2007) 855–900. doi:[10.1002/flid.1430](https://doi.org/10.1002/flid.1430).
- [38] J. J. W. van der Vegt, H. van der Ven, Space-time discontinuous Galerkin finite element method with dynamic grid motion for inviscid compressible flow, *J. Comput. Phys.* 182 (2002) 546–585. doi:[10.1006/jcph.2002.7185](https://doi.org/10.1006/jcph.2002.7185).
- [39] V. A. Dobrev, T. V. Kolev, et al., MFEM: Modular finite element methods, <http://mfem.org>, 2018.
- [40] P. Amestoy, I. Duff, J.-Y. L'Excellent, J. Koster, A fully asynchronous multifrontal solver using distributed dynamic scheduling, *SIAM J. Matrix Anal. & Appl.* 23 (2001) 15–41. doi:[10.1137/S0895479899358194](https://doi.org/10.1137/S0895479899358194).
- [41] P. R. Amestoy, A. Guermouche, J.-Y. L'Excellent, S. Pralet, Hybrid scheduling for the parallel solution of linear systems, *Parallel Comput.* 32 (2006) 136–156. doi:[10.1016/j.parco.2005.07.004](https://doi.org/10.1016/j.parco.2005.07.004).
- [42] S. Balay, S. Abhyankar, M. F. Adams, J. Brown, P. Brune, K. Buschelman, L. Dalcin, V. Eijkhout, W. D. Gropp, D. Kaushik, M. G. Knepley, L. Curfman McInnes, K. Rupp, B. F. Smith, S. Zampini, H. Zhang, H. Zhang, PETSc Web page, <http://www.mcs.anl.gov/petsc>, 2016.
- [43] S. Balay, S. Abhyankar, M. F. Adams, J. Brown, P. Brune, K. Buschelman, L. Dalcin, V. Eijkhout, W. D. Gropp, D. Kaushik, M. G. Knepley, L. Curfman McInnes, K. Rupp, B. F. Smith, S. Zampini, H. Zhang, H. Zhang, PETSc Users Manual, Technical Report ANL-95/11 - Revision 3.7, Argonne National Laboratory, 2016. URL: <http://www.mcs.anl.gov/petsc>.
- [44] S. Balay, W. D. Gropp, L. Curfman McInnes, B. F. Smith, Efficient management of parallelism in object oriented numerical software libraries, in: E. Arge, A. M. Bruaset, H. P. Langtangen (Eds.), *Modern Software Tools in Scientific Computing*, Birkhäuser Press, 1997, pp. 163–202.
- [45] B. Rivière, *Discontinuous Galerkin Methods for Solving Elliptic and Parabolic Equations*, volume 35 of *Frontiers in Applied Mathematics*, Society for Industrial and Applied Mathematics, Philadelphia, 2008.